J Math Imaging Vis (2011) 40: 305–325
DOI 10.1007/s10851-011-0263-5

Image Analysis by Conformal Embedding

Oliver Fleischmann · Lennart Wietzke · Gerald Sommer

Published online: 9 February 2011

Abstract This work presents new ideas in isotropic multi-dimensional phase based signal theory. The novel approach, called the *conformal monogenic signal*, is a rotational invariant quadrature filter for extracting local features of any curved signal without the use of any heuristics or steering techniques. The *conformal monogenic signal* contains the recently introduced *monogenic signal* as a special case and combines Poisson scale space, local amplitude, direction, phase and curvature in one unified algebraic framework. The *conformal monogenic signal* will be theoretically illustrated and motivated in detail by the relation between the Radon transform and the generalized Hilbert transform. The main idea of the *conformal monogenic signal* is to lift up n-dimensional signals by *inverse stereographic projections* to a n-dimensional sphere in $\mathbb{R}^{n+1}$ where the local signal features can be analyzed with more degrees of freedom compared to the flat n-dimensional space of the original signal domain. As result, it delivers a novel way of computing the isophote curvature of signals without partial derivatives. The philosophy of the *conformal monogenic signal* is based on the idea to use the direct relation between the original signal and geometric entities such as lines, circles, hyperplanes and hyperspheres. Furthermore, the *2D conformal monogenic signal* can be extended to signals of any dimension. The main advantages of the *conformal monogenic signal* in practical applications are its compatibility with intrinsically one dimensional and special intrinsically two dimensional signals, the rotational invariance, the low computational time complexity, the easy implementation into existing software packages and the numerical robustness of calculating exact local curvature of signals without the need of any derivatives.

Keywords Unit sphere · Signal processing · Generalized Hilbert transform · Riesz transform · Radon transform · Isotropic · Local phase based signal analysis · Clifford analysis · Monogenic signal · Analytic signal · Isophote curvature · Poisson scale space · Stereographic projection · Conformal space

1 Introduction

Low level signal analysis is often the first step of many signal processing tasks. Therefore, local signal features with geometrical and structural information determine the quality of subsequent higher level processing steps. It is important not to lose or to merge any of the original signal information within the local neighborhood of the test point (point of interest). The constraints of local signal analysis are: to obtain a set of feature vectors which span the space of signals (split of identity) and to be robust against stochastic and deterministic perturbations between the actual signal and the assumed signal model. One of the fundamental problems in signal processing is a good signal representation. Such a signal representation is the local phase information which is a robust feature with respect to noise and contrast changes [6, 7, 10]. In case of image signals it is shown in [14] that

We acknowledge funding by the German Research Foundation (DFG) under the projects *SO 320/4-2* and *We 2602/5-1*.

O. Fleischmann (✉) · L. Wietzke · G. Sommer
Cognitive Systems Group, Department of Computer Science, Kiel University, Christian-Albrechts-Platz 4, 24118 Kiel, Germany
e-mail: ofl@informatik.uni-kiel.de

L. Wietzke
e-mail: lw@informatik.uni-kiel.de

G. Sommer
e-mail: gs@informatik.uni-kiel.de

the original signal can be recovered to a fairly large extend by using only its phase information while setting its amplitude information to unity. In contrast to that, if only the amplitudes are obtained and the phases are set to zero, the recovered image signal is completely indiscernible. Therefore, phase based signal processing has found success in many applications, such as seismic data analysis in geophysics [13], disparity estimation of stereo [7], matching [1], face recognition [20] and optical flow estimation [11, 21].

2 Related Work

Phase based image processing is motivated by one-dimensional phase based signal processing where one seeks for a way to obtain the local linear phase $\phi \in [0, 2\pi]$ and local amplitude $a \in \mathbb{R}$ of a one-dimensional signal

$$f(x) = a\cos(kx + \phi) \tag{1}$$

with $x \in \mathbb{R}, k \in \mathbb{R}_+$. Gabor proposed to solve this problem by constructing the complex valued analytic signal

$$f_A(x) = f(x) + i\mathcal{H}[f](x) \tag{2}$$

where $\mathcal{H}[\cdot]$ denotes the one-dimensional Hilbert transform [8]. Since the Hilbert transform anti-commutes with the reflection $f(x) \to f(-x)$ [16], the analytic signal of the one-dimensional signal model (1) reads

$$f_A(x) = a(\cos(kx + \phi) + i\sin(kx + \phi)) \tag{3}$$

such that the features local phase and local amplitude are obtained as

$$\phi(x) = \arctan\left(\frac{\mathcal{H}[f](x)}{f(x)}\right), \tag{4}$$

$$a(x) = \sqrt{f(x)^2 + \mathcal{H}[f](x)^2}. \tag{5}$$

With this transformation in mind, Felsberg and Sommer constructed a two-dimensional generalization of the analytic signal in [4], called the monogenic signal. Assume the real part of a two-dimensional plane wave

$$f(\mathbf{x}) = a\cos(k\langle \mathbf{u}, \mathbf{x}\rangle + \phi) \tag{6}$$

is given, where $\langle\cdot,\cdot\rangle$ denotes the standard inner product in $\mathbb{R}^n$

$$\langle \mathbf{a}, \mathbf{b}\rangle = \sum_{i=1}^{n} a_i b_i \quad \text{for } \mathbf{a}, \mathbf{b} \in \mathbb{R}^n \tag{7}$$

and $\mathbf{x} \in \mathbb{R}^2$, $\mathbf{u} = (\sin(\theta), \cos(\theta))^T \in \mathbb{R}^2$. One seeks for a way to obtain, in addition to the local phase and the local amplitude, the local orientation of the plane wave. The authors propose the construction of the quaternion valued monogenic signal $f_M(\mathbf{x})$ in terms of the so called Riesz transforms in $\mathbb{R}^2$, which we will also refer to as generalized Hilbert transforms, as

$$f_M(\mathbf{x}) = f(\mathbf{x}) + i\mathcal{H}^1[f](\mathbf{x}) + j\mathcal{H}^2[f](\mathbf{x}) \tag{8}$$

where $\mathcal{H}^1[\cdot], \mathcal{H}^2[\cdot]$ denote the generalized Hilbert transform along the x_1 and the x_2 axes in $\mathbb{R}^2$.

The Riesz transform or generalized Hilbert transform, in $\mathbb{R}^n$ is a bounded linear operator which commutes with the translation and the dilation operator and is furthermore equivariant with respect to rotations in $\mathbb{R}^n$ [16]. Due to its linear shift-invariance, it can be written as a convolution with the kernels

$$h^i(\mathbf{x}) = \frac{\Gamma[(n+1)/2]}{\pi^{(n+1)/2}} \frac{x_i}{|\mathbf{x}|} \tag{9}$$

such that

$$\mathcal{H}^i[f](\mathbf{x}) = (f * h^i)(\mathbf{x}) \tag{10}$$

with the convolution given by

$$(f * h^i)(\mathbf{x}) = \int_{\mathbb{R}^n} f(\mathbf{y}) h^i(\mathbf{x} - \mathbf{y}) d\mathbf{y}. \tag{11}$$

The features local orientation, local phase and local amplitude in $\mathbb{R}^2$ are then obtained as

$$\theta(\mathbf{x}) = \arctan\left(\frac{\mathcal{H}^2[f](\mathbf{x})}{\mathcal{H}^1[f](\mathbf{x})}\right), \tag{12}$$

$$\phi(\mathbf{x}) = \arctan 2\left(\sqrt{\mathcal{H}^1[f](\mathbf{x})^2 + \mathcal{H}^2[f](\mathbf{x})^2}, f(\mathbf{x})\right), \tag{13}$$

$$a(\mathbf{x}) = \sqrt{f(x)^2 + \mathcal{H}^1[f](\mathbf{x})^2 + \mathcal{H}^2[f](\mathbf{x})^2} \tag{14}$$

with

$$\arctan 2(x_1, x_2) \tag{15}$$

$$= \begin{cases} \arctan(\frac{x_1}{x_2}) & x_2 > 0, \\ \pi + \arctan(\frac{x_1}{x_2}) & x_1 \geq 0, x_2 < 0, \\ -\pi + \arctan(\frac{x_1}{x_2}) & x_1 < 0, x_2 < 0, \\ \frac{\pi}{2} & x_1 > 0, x_2 = 0, \\ -\frac{\pi}{2} & x_1 < 0, x_2 = 0, \\ \text{undefined} & x_1 = 0, x_2 = 0. \end{cases} \tag{16}$$

The monogenic signal can be generalized to $\mathbb{R}^n$ by applying the appropriate generalized Hilbert transforms in $\mathbb{R}^n$ according to definition (10).

Most natural images locally consist of superpositions of plane waves. Since the monogenic signal is only able to extract the mentioned features for single plane waves of one

frequency, the input signal has to be filtered to suppress the unwanted frequencies. Such filters are provided as bandpass filters in the Poisson scale-space (see [5] for details). The monogenic signal is embedded in the Poisson scale space by convolving its components with the Poisson kernel in the upper half space $\mathbb{R}^3_+$ given by

$$p_s(\mathbf{x}) = \frac{\Gamma[(n+1)/2]}{\pi^{(n+1)/2}} \frac{s}{(|\mathbf{x}|^2 + s^2)^{(n+1)/2}} \tag{17}$$

with $s \in \mathbb{R}_+$, such that

$$f^s_M(\mathbf{x}) = \mathcal{P}_s[f](\mathbf{x}) + i\mathcal{P}_s[\mathcal{H}^1[f]](\mathbf{x}) + j\mathcal{P}_s[\mathcal{H}^2[f]](\mathbf{x}) \tag{18}$$

where the convolution is given by

$$\mathcal{P}_s[f](\mathbf{x}) = (f * p_s)(\mathbf{x}) = \int_{\mathbb{R}^3} f(\mathbf{y}) p_s(\mathbf{x} - \mathbf{y}) d\mathbf{y}. \tag{19}$$

The convolution of the generalized Hilbert transform kernels and the Poisson kernel leads to the conjugate Poisson kernels given by

$$q^i_s(\mathbf{x}) = \frac{\Gamma[(n+1)/2]}{\pi^{(n+1)/2}} \frac{x_i}{(|\mathbf{x}|^2 + s^2)^{(n+1)/2}} \tag{20}$$

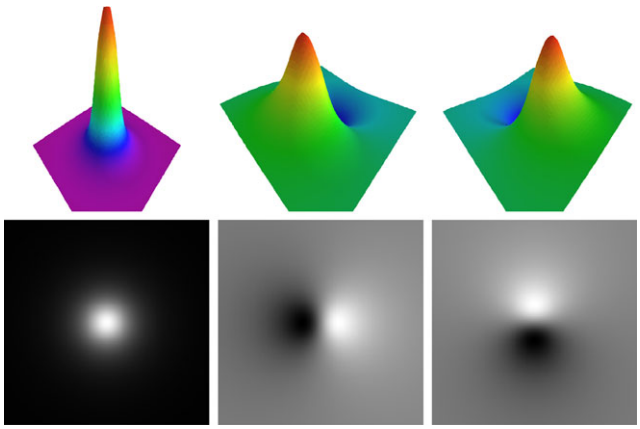

Fig. 1 From left to right: Poisson convolution kernel p_s and conjugate Poisson convolution kernels q^1_s and q^2_s in spatial domain for a certain scale space parameter $s > 0$

which are also shown in Fig. 1. With the Poisson kernel and its conjugates the scale space embedding of the monogenic signal for $n = 2$ reads

$$f^s_M(\mathbf{x}) = (p_s * f)(\mathbf{x}) + i(q^1_s * f)(\mathbf{x}) + j(q^2_s * f)(\mathbf{x}) \tag{21}$$

$$= \mathcal{P}_s[f](\mathbf{x}) + i\mathcal{Q}^1_s[f](\mathbf{x}) + j\mathcal{Q}^2_s[f](\mathbf{x}). \tag{22}$$

For further details about the standard monogenic signal we refer the reader to [4] and [19].

3 The 2D Conformal Monogenic Signal

So far we introduced the analytic and the monogenic signal, two well known methods for one-dimensional and two-dimensional signal processing. The local amplitude, local orientation and local phase turned out to be invariant with respect to rotations and translations, due to the rotational equivariance and the linear shift invariance properties of the generalized Hilbert transforms in the Euclidean plane. These properties establish the monogenic signal as a powerful feature representation. Nonetheless it is limited to the class of intrinsically one-dimensional signals. It can not capture information about neither superimposed intrinsically one-dimensional signals nor curved signals (see Fig. 2). For the first case we proposed a solution in [19]. The aim of this paper is to extend the signal model and find a solution for the second case.

3.1 Curved Signal Modeling

Two-dimensional signals are classified into local regions $N \subseteq \mathbb{R}^2$ of different intrinsic dimensions as shown in Fig. 3 [22] (which correspond to their codimension). The intrinsic dimension expresses the number of degrees of freedom necessary to describe local structure. Constant signals are of intrinsic dimension zero (i0D), straight lines and edges are of intrinsic dimension one (i1D) and all other possible patterns

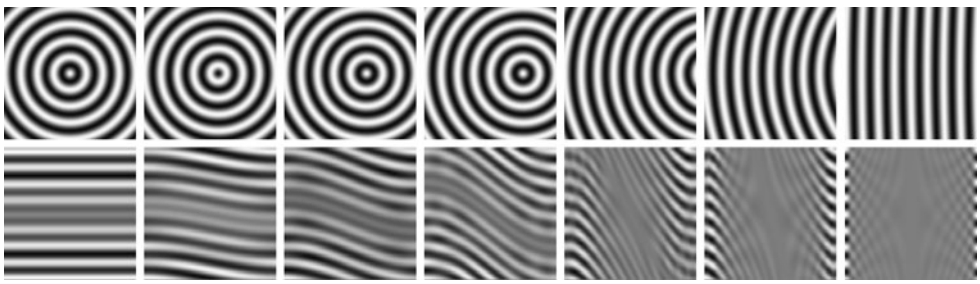

Fig. 2 From left to right: signal with varying curvature in spatial domain (*top row*) and in the corresponding 2D Radon space (*bottom row*). The 2D Radon space is too flat for analyzing and parameterizing the orientation and curvature of signals. Therefore, the dimension of the 2D Radon space must be extended to 3D

Fig. 3 From left to right: a constant signal (i0D), an arbitrary rotated 1D signal (i1D) and an i2D checkerboard signal consisting of two simple superimposed i1D signals. A curved i2D signal and two superimposed curved i2D signals. Note that all signals displayed here preserve their intrinsic dimension globally

such as corners and junctions are of intrinsic dimension two (i2D)

$$\mathrm{i0D} = \left\{ f : f(\mathbf{x}_i) = f\left(\mathbf{x}_j\right) \ \forall \mathbf{x}_i, \mathbf{x}_j \in N \right\}, \tag{23}$$

$$\mathrm{i1D} = \{ f : f(\mathbf{x}) = g(\langle \mathbf{x}, \boldsymbol{\xi} \rangle) \ \forall \mathbf{x} \in N \} \setminus \mathrm{i0D}, \tag{24}$$

$$\mathrm{i2D} = L^2(\mathbb{R}^2) \setminus (\mathrm{i0D} \cup \mathrm{i1D}) \tag{25}$$

where $\langle \cdot, \cdot \rangle$ denotes the inner product in $\mathbb{R}^2$ and $g \in L^2(\mathbb{R})$, $\boldsymbol{\xi} \in \mathbb{R}^2$, $|\boldsymbol{\xi}| = 1$. In general, i2D signals can only be modeled by an infinite number of superposed i1D signals. Therefore, it is essential to assume a certain signal model or a set of certain models for exact i2D signal analysis. Furthermore, the intrinsic dimension also depends on the scale space parameter $s \in \mathbb{R}_+$ at which the signal will be considered locally. The standard monogenic signal in the Euclidean plane is limited to the analysis of i1D signals as illustrated in Fig. 2. To analyze a broader class of signal structures we extend our signal model and include, in addition to i1D signals, curved i2D signals of the type

$$f_{\mathbf{m}}(\mathbf{x}) = a \cos(k|\mathbf{x} - \mathbf{m}| + \phi) \in \mathrm{i1D} \cup \mathrm{i2D} \tag{26}$$

where $\mathbf{m} = r_{\mathbf{m}}(\cos(\theta_{\mathbf{m}}), \sin(\theta_{\mathbf{m}}))^T \in \mathbb{R}^2$, $\mathbf{x} \in \mathbb{R}^2, r_{\mathbf{m}} \in \mathbb{R}_+, a \in \mathbb{R}, k \in \mathbb{R}_+, \phi \in [0, 2\pi]$. These are circular signals with amplitude a, frequency k and linear phase shift ϕ depending only on the distance from the center $\mathbf{m}$, which has direction $\theta_{\mathbf{m}}$ and distance $r_{\mathbf{m}}$ from the origin. We notice that these signals are constant along all circles around $\mathbf{m}$, which constitute the isophotes of the signal, in contrast to the i1D signals which are constant along all straight lines with a certain orientation. In the following it will turn out that this curved signal model contains the i1D signals as a subset such that the new model extends the former i1D signal model.

With respect to our new model for curved image structures, we have to ask for the properties of the this signal type. Analogously to i1D signals the curved signals carry a direction information induced by the angular part $\theta_{\mathbf{m}}$ of the center $\mathbf{m}$. Furthermore, with respect to the origin in $\mathbb{R}^2$, the circular signal carries a new type of information, the curvature of its isophotes. An isophote $\gamma_{\mathbf{m}}(\mathbf{x})$ of $f_{\mathbf{m}}$ at $\mathbf{x} \in \mathbb{R}^2$ is given by

$$\gamma_{\mathbf{m}}(\mathbf{x}) = \{ \mathbf{y} \in \mathbb{R}^2 : |\mathbf{x} - \mathbf{m}| = |\mathbf{y} - \mathbf{m}| \} \tag{27}$$

which is a circle around the center $\mathbf{m}$ with radius $|\mathbf{x} - \mathbf{m}|$. From differential geometry we know, that the curvature of a planar curve $\alpha(t) : \mathbb{R} \to \mathbb{R}^2$ is described by the relation $\kappa(t) = \frac{1}{r(t)}$ where $r(t)$ is the radius of osculating circle of α at t [3]. Due to the definition of our signal model $f_{\mathbf{m}}$, the isophotes $\gamma_{\mathbf{m}}(\mathbf{x})$ are circles around $\mathbf{m}$, such that the osculating circles of the isophotes are the isophotes themselves. Therefore, the curvature $\kappa_{\mathbf{m}}(\mathbf{x})$ of an isophote $\gamma_{\mathbf{m}}(\mathbf{x})$ passing through a point of interest $\mathbf{x}$ is obtained as

$$\kappa_{\mathbf{m}}(\mathbf{x}) = \frac{1}{r_{\mathbf{m}}(\mathbf{x})} = \frac{1}{|\mathbf{x} - \mathbf{m}|}. \tag{28}$$

Classical differential geometry yields the result, that for a signal $f \in L^2(\mathbb{R}^2)$ the isophote curvature at a point $\mathbf{x} \in \mathbb{R}^2$ reads (see e.g. [12])

$$\kappa = \frac{-\frac{\partial^2}{\partial x^2} f (\frac{\partial}{\partial y} f)^2 + 2 \frac{\partial}{\partial x} f \frac{\partial}{\partial y} f \frac{\partial^2}{\partial xy} f - \frac{\partial^2}{\partial y^2} f (\frac{\partial}{\partial x} f)^2}{((\frac{\partial}{\partial x} f)^2 + (\frac{\partial}{\partial y} f)^2)^{\frac{3}{2}}}. \tag{29}$$

The classical method has been used in various image processing applications, see e.g. [18] and [17]. In the following we introduce a novel method to obtain the curvature $\kappa_{\mathbf{m}}(\mathbf{x})$ of a signal $f_{\mathbf{m}}$ at position $\mathbf{x} \in \mathbb{R}^2$ within our framework of generalized Hilbert transforms without using partial derivatives of any order. Furthermore we will still be able to obtain the local orientation, local amplitude and, in the case of certain signals, the local phase of our circular signal within one single signal representation. We will show that i1D signals are already included as a subset in our new signal representation such that we will not lose the properties of the classical monogenic signal.

3.2 Conformal Embedding

As a first step of our novel method we will investigate how we can obtain the radius of single isophotes of a circular input signal $f_{\mathbf{m}}$. Let us fix an isophote $\gamma_{\mathbf{m}}(\mathbf{x})$ of a circular signal $f_{\mathbf{m}}$ passing through $\mathbf{x} \in \mathbb{R}^2$. Without loss of generalization we choose a new coordinate system in $\mathbb{R}^2$ with $\mathbf{x}$ as its origin. We will leave the Euclidean plane $\mathbb{R}^2$ and embed our isophote on the sphere

$$\mathbb{S}^2 := \left\{ \mathbf{u} \in \mathbb{R}^3 : u_1^2 + u_2^2 + \left(u_3 - \frac{1}{2}\right)^2 = \frac{1}{4} \right\} \tag{30}$$

which is the sphere with center $(0, 0, \frac{1}{2})^T$ and radius $\frac{1}{2}$. The sphere $\mathbb{S}^2$ touches the Euclidean plane $\mathbb{R}^2$ such that its south-pole coincides with the origin $(0, 0, 0)^T$. The embedding of the isophote $\gamma_{\mathbf{m}}(\mathbf{x})$ is established by the application of the inverse stereographic projection from $\mathbb{R}^2$ to $\mathbb{S}^2$ given

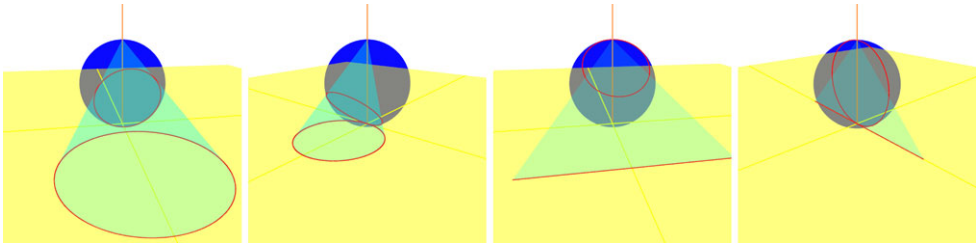

Fig. 4 From left to right: The first two figure plane being mapped to circles not passing through the north pole $(0, 0, 1)$ of the sphere and the next two figure mapped to circles passing through the north pole of the sphere, i.e. lines are a special case of circles with infinite radius

by

$$\mathcal{S}^{-1}(\mathbf{x}) = \frac{1}{1 + x_1^2 + x_2^2} \begin{pmatrix} x_1 \\ x_2 \\ x_1^2 + x_2^2 \end{pmatrix} \tag{31}$$

for $\mathbf{x} = (x_1, x_2)^T \in \mathbb{R}^2$ whereas the stereographic projection from $\mathbb{S}^2$ to $\mathbb{R}^2$ is given by

$$\mathcal{S}(\omega) = \frac{1}{1 - \omega_3} \begin{pmatrix} \omega_1 \\ \omega_2 \end{pmatrix} \tag{32}$$

for ω in $\mathbb{S}^2$. The goal is now to obtain the curvature of the isophote $\gamma_{\mathbf{m}}(\mathbf{x})$ of $f_{\mathbf{m}}$ passing through $\mathbf{x}$.

3.3 Properties of the Stereographic Projection

To explain the geometric idea of our curvature calculation method, we first discuss some important properties of the inverse stereographic projection. The inverse stereographic projection is a conformal mapping from $\mathbb{R}^2$ to $\mathbb{S}^2$. It has the properties, that it preserves angles and maps circles in the Euclidean plane to circles on $\mathbb{S}^2$. The first property is important for us, since the embedding preserves the direction angle $\theta_{\mathbf{m}}$ of our signal $f_{\mathbf{m}}$ induced by the direction of the center $\mathbf{m}$ of the signal. The second property is important for us, since it allows us to treat the two signal types, i1D and curved signals in the plane, as the same type on the sphere: circles. A straight line in the Euclidean plane can be interpreted as a circle with infinite radius. Since the inverse stereographic projection maps circles in the plane to circles on the sphere, not only circles with finite radius, but also straight lines map to circles on the sphere. Since the north-pole represents the point at infinity, all straight lines in $\mathbb{R}^2$ map to circles on $\mathbb{S}^2$ passing through the north-pole $(0, 0, 1)$. Since we have identified the south-pole of $\mathbb{S}^2$ with the origin of $\mathbb{R}^2$, straight lines through the origin map to great circles through the north- and the south-pole. Circles with finite radius through the origin in $\mathbb{R}^2$ map to circles through the south-pole of $\mathbb{S}^2$. In addition, the direction angles in the plane are preserved by the inverse stereographic projection, such that both structure types retain their direction in the case of curved signals and their orientation in the case of i1D signals after the mapping. Figure 4 illustrates both scenarios.

3.4 Circles as Plane-Sphere Intersections

Now that we can describe straight lines and circles in the plane as circles on the sphere, we make the important observation that we can also describe both of these structures as intersections of the sphere $\mathbb{S}^2$ with a two-dimensional plane in $\mathbb{R}^3$, since every circle on $\mathbb{S}^2$ results from the intersection of the sphere with a plane. If we restrict our analysis to the isophotes passing through the origin, we know that these map to circles through the south-pole of $\mathbb{S}^2$. In the case of straight lines they map to great circles additionally passing through north-pole. Now consider the isophote $\gamma_{\mathbf{m}}(\mathbf{x})$ which is projected to $\mathbb{S}^2$ as

$$\mathcal{S}^{-1}(\gamma_{\mathbf{m}}(\mathbf{x})) = \{\mathcal{S}^{-1}(\mathbf{y}) : \mathbf{y} \in \gamma_{\mathbf{m}}(\mathbf{x})\}. \tag{33}$$

There exists a plane $\mathbf{P}_{\mathbf{m}}$ such that the projected isophote $\mathcal{S}^{-1}(\gamma_{\mathbf{m}}(\mathbf{x}))$ is equal to the intersection of the sphere and $\mathbf{P}_{\mathbf{m}}$

$$\mathcal{S}^{-1}(\gamma_{\mathbf{m}}(\mathbf{x})) = \mathbf{P}_{\mathbf{m}} \cap \mathbb{S}^2. \tag{34}$$

A plane in $\mathbb{R}^3$ is characterized by its unit normal vector $\mathbf{n}_{\mathbf{m}}$ and its distance $d_{\mathbf{m}}$ from the origin. For the plane $\mathbf{P}_{\mathbf{m}}$ we know that it passes through the origin since the south-pole $(0, 0, 0)^T$ is contained in $\mathbf{P}_{\mathbf{m}} \cap \mathbb{S}^2$. It follows that $(0, 0, 0)^T \in \mathbf{P}_{\mathbf{m}}$. Therefore, it follows that $d_{\mathbf{m}} = 0$. We conclude that an isophote $\gamma_{\mathbf{m}}(\mathbf{x})$ is uniquely described by the normal vector $\mathbf{n}_{\mathbf{m}}$ of the corresponding plane $\mathbf{P}_{\mathbf{m}}$. We will show in the next section how this normal vector $\mathbf{n}_{\mathbf{m}}$ and therefore the plane $\mathbf{P}_{\mathbf{m}}$ actually looks like and how it relates to our chosen isophote $\gamma_{\mathbf{m}}$.

Figure 4 shows several possible isophotes $\gamma_{\mathbf{m}}$ and their projections to $\mathbb{S}^2$. Notice that the first two belong to the class of curved isophote, whereas the second two are straight lines. For all curves a coordinate system is chosen in such a way, that the south-pole of the sphere coincides with the origin of this new coordinate system. The projection of the isophote through the origin is then described by the intersection of a plane and $\mathbb{S}^2$.

3.5 Geometric Interpretation of the Normal Vector

Since an isophote $\gamma_{\mathbf{m}}(\mathbf{x})$ is uniquely described by the corresponding normal vector $\mathbf{n}_{\mathbf{m}}$, all the properties of the isophote are encoded in the normal vector $\mathbf{n}_{\mathbf{m}}$. The properties we are interested in are the direction $\theta_{\mathbf{m}}$ of $\mathbf{m}$ with respect to $\mathbf{x}$ and the radius $r_{\mathbf{m}}$ of the isophote passing through $\mathbf{x}$, which is equal to the distance $|\mathbf{x}-\mathbf{m}|$. Figure 5 shows the geometric relationship between the isophote and its projection to $\mathbb{S}^2$. We formulate our result as:

Theorem 1 *Let* $\mathbf{x}\in\mathbb{R}^2$, $\mathbf{m}\in\mathbb{R}^2$, $\theta_{\mathbf{m}}\in[0,2\pi]$ *with*

$$\mathbf{m}=\mathbf{x}+r_{\mathbf{m}}(\cos(\theta_{\mathbf{m}}),\sin(\theta_{\mathbf{m}}))^T \tag{35}$$

where $r_{\mathbf{m}}=|\mathbf{x}-\mathbf{m}|$. *Let* $\gamma_{\mathbf{m}}(\mathbf{x})$ *denote the isophote of a signal* $f_{\mathbf{m}}$ *through* $\mathbf{x}$ *and let* $\mathbf{P}_{\mathbf{m}}$ *denote the plane which fulfills* $\mathcal{S}^{-1}(\gamma_{\mathbf{m}}(\mathbf{x}))=\mathbf{P}_{\mathbf{m}}\cap\mathbb{S}^2$ *with normal vector*

$$\mathbf{n}_{\mathbf{m}}=\begin{pmatrix}n_{\mathbf{m},1}\\ n_{\mathbf{m},2}\\ n_{\mathbf{m},3}\end{pmatrix}=\begin{pmatrix}\sin(\varphi)\cos(\theta)\\ \sin(\varphi)\sin(\theta)\\ \cos(\varphi)\end{pmatrix}. \tag{36}$$

Then it holds that

$$\varphi=\arctan(2|\mathbf{x}-\mathbf{m}|)=\arctan(2r_{\mathbf{m}}) \tag{37}$$

$$=\arccos\left(\frac{1}{\sqrt{1+4r_{\mathbf{m}}^2}}\right) \tag{38}$$

and

$$\theta=\theta_{\mathbf{m}}. \tag{39}$$

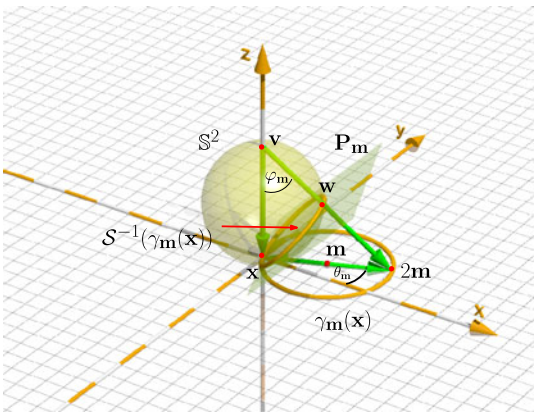

Fig. 5 Illustration of an isophote $\gamma_{\mathbf{m}}(\mathbf{u})$ and its projection $\mathcal{S}^{-1}(\gamma_{\mathbf{m}}(\mathbf{u}))$ to $\mathbb{S}^2$. The radius $|\mathbf{m}-\mathbf{x}|=r_{\mathbf{m}}$ can be calculated from the angle $\varphi_{\mathbf{m}}$ as $\tan\varphi_{\mathbf{m}}=2|\mathbf{m}|$. Therefore $\varphi_{\mathbf{m}}$ can be obtained from the normal vector of $\mathbf{P}_m$

Proof By Thales theorem we find that

$$\begin{pmatrix}2m_1-x_1\\ 2m_2-x_2\\ 1\end{pmatrix}\perp\mathbf{P}_m \tag{40}$$

such that

$$\mathbf{n}_{\mathbf{m}}=\frac{1}{\sqrt{1+4r_{\mathbf{m}}^2}}\begin{pmatrix}2m_1-x_1\\ 2m_2-x_2\\ 1\end{pmatrix} \tag{41}$$

$$=\begin{pmatrix}2r_{\mathbf{m}}\cos(\theta_{\mathbf{m}})\\ 2r_{\mathbf{m}}\sin(\theta_{\mathbf{m}})\\ 1\end{pmatrix}=\begin{pmatrix}\sin(\varphi_{\mathbf{m}})\cos(\theta_{\mathbf{m}})\\ \sin(\varphi_{\mathbf{m}})\sin(\theta_{\mathbf{m}})\\ \cos(\varphi_{\mathbf{m}})\end{pmatrix} \tag{42}$$

which concludes the proof. □

3.6 Isophote Properties

The theorem is the central idea of our curvature estimation method. It shows, that it is possible to obtain the direction angle $\theta_{\mathbf{m}}$ of the center $\mathbf{m}$ with respect to $\mathbf{x}$ and the radius $r_{\mathbf{m}}$ of the isophote of $f_{\mathbf{m}}$ passing through $\mathbf{x}$ just from components of the normal vector $\mathbf{n}_{\mathbf{m}}$ of the plane $\mathbf{P}_{\mathbf{m}}$ as:

Corollary 1 (Isophote curvature)

$$\kappa_{\mathbf{m}}=\frac{1}{r_{\mathbf{m}}}=\frac{1}{|\mathbf{x}-\mathbf{m}|}=\frac{2n_{\mathbf{m},3}}{\sqrt{n_{\mathbf{m},1}^2+n_{\mathbf{m},2}^2}}. \tag{43}$$

Corollary 2 (Isophote direction)

$$\theta_{\mathbf{m}}=\arctan 2(n_{\mathbf{m},2},n_{\mathbf{m},1}). \tag{44}$$

3.7 Isophote Classification

The two important properties isophote curvature and isophote direction are encoded in the normal vector of the plane $\mathbf{P}_{\mathbf{m}}$. Apart from obtaining these properties, we are also able to decide whether an isophote is a straight line, which corresponds to a circle with an infinite radius, or a circle with a finite radius. Let $\gamma_{\mathbf{m}}$ denote an isophote with an infinite radius modeled by a center $\mathbf{m}$ with infinite distance from the origin:

$$\mathbf{m}=\lim_{r_{\mathbf{m}}\to\infty} r_{\mathbf{m}}(\cos(\theta_{\mathbf{m}}),\sin(\theta_{\mathbf{m}}))^T. \tag{45}$$

Then the projection $\mathcal{S}^{-1}(2\mathbf{m})$ coincides with the north-pole such that the angle $\varphi_{\mathbf{m}}$ approaches $\pi/2$ and $\cos(\varphi_{\mathbf{m}})$ vanishes. It follows that the normal vector $\mathbf{n}_{\mathbf{m}}$ of the plane $\mathbf{P}_{\mathbf{m}}$ describing $\mathcal{S}^{-1}(\gamma_{\mathbf{m}}(\mathbf{x}))$ is obtained as $\mathbf{n}_{\mathbf{m}}=(\cos(\theta_{\mathbf{m}}),\sin(\theta_{\mathbf{m}}),0)^T$. For every isophote with finite radius, the angle $\cos(\varphi_{\mathbf{m}})$ does not vanish. We can therefore

distinguish between straight lines and curved isophotes by examining the third component $n_{\mathbf{m},3}$ of the normal vector $\mathbf{n_m}$.

So far we developed a method which is able distinguish between straight line and curved isophotes and to obtain the curvature and the direction of the isophote by its normal vector $\mathbf{n_m}$, corresponding to the plane passing through the projected isophote on $\mathbb{S}^2$. The problem of isophote curvature estimation is therefore equivalent to the estimation of the normal vector $\mathbf{n_m}$. The method has been developed for single isolated isophotes as illustrated in Fig. 4, but actually we do not know the isophotes in advance. Hence we are not able to project a single isolated isophote to $\mathbb{S}^2$. Instead we always project a local neighborhood of our signal $f_\mathbf{m}$ with respect to our point of interest to $\mathbb{S}^2$. Consequently we are faced with the problem of estimating the normal vector $\mathbf{n_m}$, which is the key to the curvature information, from our projected neighborhood around $\mathbf{x}$. We will introduce a method which will estimate the normal vector $\mathbf{n_m}$ from the projected signal using the generalized Hilbert transforms in $\mathbb{R}^3$ such that a curvature estimation according to Theorem 1 will be possible.

3.8 Relationship Between the Generalized Hilbert Transform and the Radon Transform

It is well known from the two dimensional setting, that the close relationship between the generalized Hilbert transforms and the Radon transform provides an intuitive interpretation of the generalized Hilbert transforms for plane wave signals (see e.g. [19]). The orientation of plane waves in $\mathbb{R}^3$ is, just as our plane $\mathbf{P_m}$, characterized by a single normal vector in $\mathbb{R}^3$. We will establish a link between the normal vector of our plane $\mathbf{P_m}$ describing a projected isophote, and the orientation vector of a plane wave in $\mathbb{R}^3$ using the relationship between the generalized Hilbert transforms and the Radon transform. We will introduce a novel signal model, called the conformal monogenic signal, and justify its construction by the Radon transform in $\mathbb{R}^3$. The Radon transform in $\mathbb{R}^n$ is an integral transform integrating a function over all $n-1$ dimensional hyperplanes in $\mathbb{R}^n$ which is defined as:

Definition 1 (Radon transform) Let $f \in L^2(\mathbb{R}^n)$, $\boldsymbol{\xi} \in \mathbb{R}^n$, $|\boldsymbol{\xi}| = 1, t \in \mathbb{R}$. Then the Radon transform of f is defined as

$$\mathcal{R}[f](\boldsymbol{\xi}, t) = \int_{\mathbb{R}^n} f(\mathbf{u})\delta(t - \langle \boldsymbol{\xi}, \mathbf{u}\rangle) d\mathbf{u}. \tag{46}$$

The inversion of the Radon transform in $\mathbb{R}^n$ reads

$$f(\mathbf{u}) = \frac{1}{2}(2\pi)^{1-n}(-1)^{(n-1)/2} \cdot \int_{|\boldsymbol{\xi}|=1} \frac{\partial^{n-1}}{\partial t^{n-1}} \mathcal{R}[f](\boldsymbol{\xi}, \langle \boldsymbol{\xi}, \mathbf{u}\rangle)\, d\boldsymbol{\xi} \tag{47}$$

if n is odd, and

$$f(\mathbf{u}) = (2\pi)^{-n}(-1)^{n/2} \cdot \int_{-\infty}^{\infty} \frac{1}{q} \int_{|\boldsymbol{\xi}|=1} \frac{\partial^{n-1}}{\partial t^{n-1}} \mathcal{R}[f](\boldsymbol{\xi}, \langle \boldsymbol{\xi}, \mathbf{u}\rangle + q)\, d\boldsymbol{\xi}\, dq \tag{48}$$

if n is even.

It integrates over all hyperplanes with normal vector $\boldsymbol{\xi}$ and distance t from the origin. The parameter space of the Radon transform in $\mathbb{R}^3$ is therefore spanned by the two angles (φ, θ) describing the unit normal vector of the plane and its distance t from the origin. For a fixed unit normal vector $\boldsymbol{\xi}$, $\mathcal{R}[f](\boldsymbol{\xi}, \cdot)$ describes a one-dimensional function in Radon domain which we will refer to as a slice. We are interested in the Radon transform of the real part of a three dimensional plane wave in $\mathbb{R}^3$ with orientation vector $\boldsymbol{\omega}$, $|\boldsymbol{\omega}| = 1$, amplitude $a \in \mathbb{R}$, frequency $k \in \mathbb{R}_+$ and linear phase shift $\phi \in [0, 2\pi]$ given by

$$\psi(\mathbf{u}) = a\cos(k\langle \mathbf{u}, \boldsymbol{\omega}\rangle + \phi), \quad \mathbf{u} \in \mathbb{R}^3. \tag{49}$$

For the Radon transform to be well defined we require ψ to vanish at infinity. So we embed it in the Poisson scale space in $\mathbb{R}^4_+$ as

$$\psi_s(\mathbf{u}) = \mathcal{P}_s[\psi](\mathbf{u}), \quad s \in \mathbb{R}_+. \tag{50}$$

Its Radon transform results in

$$\mathcal{R}[\psi_s](\boldsymbol{\xi}, t) = \begin{cases} a\,\mathcal{P}_s^{1D}[\cos(\cdot)](k\,t + \phi) & \text{for } \boldsymbol{\xi} = \boldsymbol{\omega}, \\ c & \text{else}, \end{cases} \tag{51}$$

where $c \in \mathbb{R}$ is a constant and $\mathcal{P}_s^{1D}[\cdot] : L^2(\mathbb{R}) \to L^2(\mathbb{R})$ with

$$\mathcal{P}_s^{1D}[f](t) = (p_s * f)(t) \tag{52}$$

denotes the one-dimensional Poisson transform along a single slice which is the one-dimensional convolution with the Poisson kernel p_s on the real line given by (17) for $n = 1$. We notice that the Radon transform of ψ_s is only non-constant along the slice defined by the parameters (φ, θ) corresponding to the orientation vector $\boldsymbol{\omega}$. The generalized Hilbert transform and the Radon transform in $\mathbb{R}^3$ are related due to

Corollary 3 (Relationship between the Radon transform and the generalized Hilbert transform) *Let* $f \in L^2(\mathbb{R}^n)$, $\boldsymbol{\xi} \in \mathbb{R}^n$, $|\boldsymbol{\xi}| = 1, t \in \mathbb{R}, i \in \{1, \ldots, n\}$. *Then it holds that*

$$\mathcal{R}[\mathcal{H}^i[f]](\boldsymbol{\xi}, t) = \xi_i \mathcal{H}^{1D}[\mathcal{R}[f](\boldsymbol{\xi}, \cdot)](t) \tag{53}$$

where $\mathcal{H}^{1D}[\cdot] : L^2(\mathbb{R}) \to L^2(\mathbb{R})$ *denotes the one- dimensional Hilbert transform along* t *for a fixed slice at* $\boldsymbol{\xi}$ *in the*

Radon domain given by the convolution

$$\mathcal{H}^{1D}[f](t) = (h * f)(t) \tag{54}$$

with the Hilbert transform kernel h on the real line given by (9) *for* $n = 1$.

In terms of the Radon transform, the generalized Hilbert transforms $\mathcal{H}^i[\cdot]$ perform a Radon transform, apply a one dimensional Hilbert transform along every slice indicated by the normal vector $\boldsymbol{\xi}$, multiply every slice with the i-th component ξ_i of the normal vector and transform the result back with the inverse Radon transform. This result is of importance with respect to our plane wave model ψ_s in $\mathbb{R}^3$. Consider the Radon transform of the generalized Hilbert transforms in $\mathbb{R}^3$ applied to ψ_s

$$\mathcal{R}[\mathcal{H}^i[\psi_s]](\boldsymbol{\xi}, t) = \xi_i \, \mathcal{H}^{1D}[\mathcal{R}[\psi_s](\boldsymbol{\xi}, \cdot)](t). \tag{55}$$

Due to (51) it follows that

$$\mathcal{R}[\mathcal{H}^i[\psi_s]](\boldsymbol{\xi}, t), \tag{56}$$

$$= \begin{cases} \omega_i \mathcal{H}^{1D}[\mathcal{P}_s^{1D}[\cos(\cdot)]](kt + \phi) & \text{for } \boldsymbol{\xi} = \boldsymbol{\omega}, \\ 0 & \text{else}, \end{cases} \tag{57}$$

where we used the fact, that the Hilbert transform of a cosine wave is a sine wave with the same frequency, amplitude and phase and the Hilbert transform of a constant function is zero. If we now apply the inverse Radon transform, the inversion integral depends only on the normal vector $\boldsymbol{\xi} = \boldsymbol{\omega}$ such that

$$\mathcal{H}^i[\psi_s](\mathbf{u}) = \mathcal{Q}_s^i[\psi](\mathbf{u}) \tag{58}$$

$$= \mathcal{R}^{-1}[\mathcal{R}[\mathcal{H}^i[\psi_s]]](\mathbf{u}) \tag{59}$$

$$= \omega_i \mathcal{R}^{-1}[(\boldsymbol{\xi}, t) \mapsto \mathcal{H}^{1D}[\mathcal{R}[\psi_s](\boldsymbol{\xi}, \cdot)](t)](\mathbf{u}). \tag{60}$$

We notice that the partial generalized Hilbert transforms of ψ_s are equal up to the angular factor ω_i. This is an important consequence, since we are now able to extract the local angles at a point of interest $\mathbf{u} \in \mathbb{R}^3$ describing the orientation vector $\boldsymbol{\omega}$ of the plane wave ψ_s from the generalized Hilbert transform as

$$\theta(\mathbf{u}) = \arctan 2(\mathcal{H}^2[\psi_s](\mathbf{u}), \mathcal{H}^1[\psi_s](\mathbf{u})) \tag{61}$$

and

$$\varphi(\mathbf{u}) = \arctan\left(\frac{\sqrt{\mathcal{H}^1[\psi_s](\mathbf{u})^2 + \mathcal{H}^2[\psi_s](\mathbf{u})^2}}{\mathcal{H}^3[\psi_s](\mathbf{u})}\right). \tag{62}$$

3.9 Identifying Circular Signals with Plane Waves

Actually the method introduced above to extract the angles of interest only holds for plane waves ψ_s in $\mathbb{R}^3$. We introduced the relationship between the Radon transform and the generalized Hilbert transform with the goal in mind, to identify the projection of a circular signal $f_{\mathbf{m}}$ to $\mathbb{S}^2$ with a plane wave, such that the orientation angles of the plane wave represent the parameters of the circular signal in the plane. To establish this relationship, we first show that the projection of a circular signal approximates a certain plane wave. We define the spherical embedding $g_{\mathbf{m}}$ of the circular signal $f_{\mathbf{m}}$ with respect to a point of interest $\mathbf{x} \in \mathbb{R}^2$ as

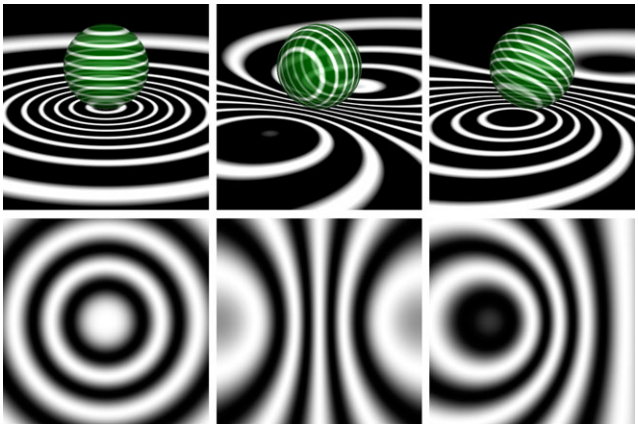

Fig. 6 Illustration of the conformal mapping of 2D signals to the 3D conformal space

$$g_{\mathbf{m}}^{\mathbf{x}}(\mathbf{u}) = \begin{cases} f_{\mathbf{m}}(\mathcal{S}(\mathbf{u}) + \mathbf{x}) & \text{for } \mathbf{u} \in \mathbb{S}^2, \\ 0 & \text{else} \end{cases} \tag{63}$$

and its Poisson scale space embedding in $\mathbb{R}^4_+$ as

$$g_{\mathbf{m}}^{\mathbf{x},s}(\mathbf{u}) = \mathcal{P}_s[g_{\mathbf{m}}^{\mathbf{x}}](\mathbf{u}) \tag{64}$$

$$= \int_{\mathbb{R}^3} g_{\mathbf{m}}^{\mathbf{x}}(\mathbf{v}) p_s(\mathbf{u} - \mathbf{v}) dm(\mathbf{v}). \tag{65}$$

Here $dm(\mathbf{v}) = \delta(|\mathbf{v} - \mathbf{c}|)d\mathbf{v}$ denotes the Radon measure for the functional $g_{\mathbf{m}}$ supported on sphere $\mathbb{S}^2$ where $\mathbf{c}$ is the center of $\mathbb{S}^2$ and $\delta(\cdot)$ is the Delta distribution. For further details on the validity of this construction we refer the reader to [23]. Note that we define this embedding with respect to a point of interest $\mathbf{x}$, since we want to analyze our signals *locally*. For each $\mathbf{x}$ we want the south-pole of the sphere to coincide with $\mathbf{x}$ such that we will evaluate all operations at the south-pole of $\mathbb{S}^2$. So actually for every $\mathbf{x}$ we consider $\mathbf{x}$ as the origin of a new coordinate system and project to $\mathbb{S}^2$ with respect to this new coordinate system such that the south-pole of $\mathbb{S}^2$ coincides with the new origin. In the following we will show that for all $\mathbf{x} \in \mathbb{R}^2$, $g_{\mathbf{m}}^{\mathbf{x},s}$ approximates a plane wave restricted to $\mathbb{S}^2$ such that the Radon transform of $g_{\mathbf{m}}^{\mathbf{x},s}$ inherits the properties of a plane wave in $\mathbb{R}^3$. Let $\mathbf{x} \in \mathbb{R}^2$ and assume a new coordinate with $\mathbf{x}$ as the origin is chosen. With respect to this fixed $\mathbf{x}$, which is the new origin, we abbreviate $g_{\mathbf{m}}^{\mathbf{x},s} = g_{\mathbf{m}}^{\mathbf{0},s} = g_{\mathbf{m}}^{s}$.

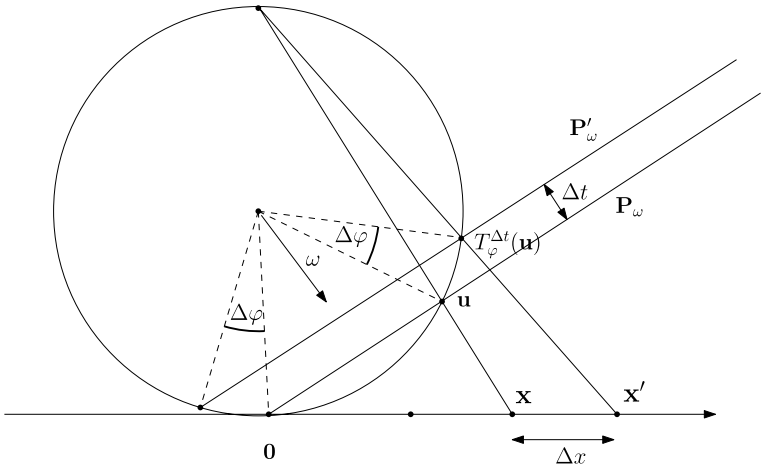

Fig. 7 Geometric illustration of the mapping T. For sufficiently small Δt we find that $\Delta x \approx \Delta t$

Theorem 2 *Let* $\mathbf{m} = r_\mathbf{m}(\cos(\theta_\mathbf{m}), \sin(\theta_\mathbf{m}))$, $r_\mathbf{m} > 0$ *and let* $f_\mathbf{m}(\mathbf{x}) = a\cos(k\,|\mathbf{m}-\mathbf{x}| + \phi)$ *denote a circular signal with center* $\mathbf{m}$, *amplitude* $a \in \mathbb{R}$, *linear phase* $\phi \in [0, 2\pi]$ *and frequency* $k \in \mathbb{R}_+$. *Let* $\psi(\mathbf{u}) = a\cos(k\langle \mathbf{u}, \boldsymbol{\omega}\rangle + k\,r_\mathbf{m} + \phi)$ *denote a plane wave in* $\mathbb{R}^3$ *with orientation vector*

$$\boldsymbol{\omega} = (\sin(\varphi_\mathbf{m})\cos(\theta_\mathbf{m}), \sin(\varphi_\mathbf{m})\sin(\theta_\mathbf{m}), \cos(\varphi_\mathbf{m}))^T \tag{66}$$

$$= \left(\frac{1}{4} + r_\mathbf{m}^2\right)^{-\frac{1}{2}} \left(r_\mathbf{m}\cos\theta_\mathbf{m}, r_\mathbf{m}\sin\theta_\mathbf{m}, \frac{1}{2}\right)^T. \tag{67}$$

Then for all $\mathbf{x} \in \mathbb{R}^2$

$$\epsilon_{min} < |f_\mathbf{m}(\mathbf{x}) - \psi(\mathcal{S}^{-1}(\mathbf{x}))| < \epsilon_{max} \tag{68}$$

where

$$\epsilon_{max} \approx |\Delta t\,(2r_\mathbf{m}(1+4r_\mathbf{m}^2)^{\frac{3}{2}} - 1)|, \tag{69}$$

$$\epsilon_{min} \approx |\Delta t\,(3r_\mathbf{m}(1+4r_\mathbf{m}^2)^{-\frac{1}{2}} - 1)| \tag{70}$$

and $\Delta t = \langle \mathcal{S}^{-1}(\mathbf{x}), \boldsymbol{\omega}\rangle$.

Proof Without loss of generalization we assume that $\mathbf{m}$ is located on the x_1 axes with $\mathbf{m} = (m_1, 0)$. Then the isophote $\gamma(\mathbf{0})$ passing through the origin is a circle with center $\mathbf{m}$ whose projection $\mathbf{C} = \mathcal{S}^{-1}(\gamma(\mathbf{0}))$ is a circle which passes through the south-pole of $\mathbb{S}^2$. Let $\psi(\mathbf{u}) = \cos(k\langle \mathbf{u}, \boldsymbol{\omega}\rangle + k\,r_\mathbf{m} + \phi)$ denote the plane wave in $\mathbb{R}^3$ with orientation vector

$$\boldsymbol{\omega} = (\sin(\varphi_\mathbf{m})\cos(\theta_\mathbf{m}), \sin(\varphi_\mathbf{m})\sin(\theta_\mathbf{m}), \cos(\varphi_\mathbf{m}))^T \tag{71}$$

$$= \left(\frac{1}{4} + r_\mathbf{m}^2\right)^{-\frac{1}{2}} \left(r_\mathbf{m}\cos(\theta_\mathbf{m}), r_\mathbf{m}\sin(\theta_\mathbf{m}), \frac{1}{2}\right)^T. \tag{72}$$

There exists a plane $\mathbf{P}_{\boldsymbol{\omega}}$ with normal vector $\boldsymbol{\omega}$ whose intersection with $\mathbb{S}^2$ results in $\mathbf{C} = \mathbf{P}_{\boldsymbol{\omega}} \cap \mathbb{S}^2$. For all $\mathbf{u} \in \mathbf{C}$ we find that

$$f_\mathbf{m}(\mathcal{S}(\mathbf{u})) = \psi(\mathbf{u}) = \cos(k r_\mathbf{m} + \phi) \tag{73}$$

since $\langle \mathbf{u}, \boldsymbol{\omega}\rangle = 0$. Suppose we move the plane $\mathbf{P}_{\boldsymbol{\omega}}$ in the direction $\boldsymbol{\omega}$ by $\Delta t \in \mathbb{R}$ as (see also Fig. 7)

$$\mathbf{P}'_{\boldsymbol{\omega}} = \{\mathbf{v} + \Delta t\boldsymbol{\omega} : \mathbf{v} \in \mathbf{P}_{\boldsymbol{\omega}}\}. \tag{74}$$

We impose the restriction, that the distance of shifted plane is less than the radius of the sphere $\mathbb{S}^2$

$$0 \le \frac{\cos(\varphi)}{2} + \Delta t < \frac{1}{2} \tag{75}$$

such that the intersection $\mathbf{P}'_{\boldsymbol{\omega}} \cap \mathbb{S}^2$ is nonempty. Then for all $\mathbf{u}' \in \mathbf{C}'$ where $\mathbf{C}' = \mathbf{P}'_{\boldsymbol{\omega}} \cap \mathbb{S}^2$

$$\psi(\mathbf{u} + \Delta t\boldsymbol{\omega}) = a\cos(k(r_\mathbf{m} + \Delta t) + \phi) \tag{76}$$

since

$$\langle \mathbf{u}', \boldsymbol{\omega}\rangle = \langle \mathbf{u}, \boldsymbol{\omega}\rangle + \Delta t = \Delta t. \tag{77}$$

As expected, the argument of plane wave ψ depends linearly on the shift by Δt since we move our points of interest in the direction of its orientation vector. We will show that the shifted points back-projected to the plane and evaluated with respect to our circular signal $f_\mathbf{m}$ almost behave linearly with respect to Δt for sufficiently small Δt. To investigate how the projection of the points $\mathbf{u} \in \mathbf{C}$ behaves, if $\mathbf{C}$ is mapped to $\mathbf{C}'$, we first give the explicit construction of the corresponding mapping. Let $R_\alpha(\mathbf{u})$ denote a rotation of $\mathbf{u}$ in $\mathbb{R}^3$ around the axis $(0,1,0)^T$ by the angle α. We define the mapping $T_\alpha^{\Delta t} : \mathbf{C} \to \mathbf{C}'$ as the composition $\mathbf{u} \mapsto (T_6 \circ T_5 \circ T_4 \circ T_3 \circ T_2 \circ T_1)(\mathbf{u})$ where

(i) $T_1(\mathbf{u}) = \mathbf{u} + (0, 0, -\frac{1}{2})^T$
(ii) $T_2(\mathbf{u}) = R_\alpha(\mathbf{u})$
(iii) $T_3(\mathbf{u}) = \mathbf{u} - \Delta t(0,0,1)^T$
(iv) $T_4(\mathbf{u}) = (u_1/s, u_2/s, u_3)$ where $s = \frac{\cos(\alpha)}{\cos(\alpha)+2\Delta t}$
(v) $T_5(\mathbf{u}) = R_{-\alpha}(\mathbf{u})$
(vi) $T_6(\mathbf{u}) = \mathbf{u} + (0, 0, +\frac{1}{2})^T$.

The mapping $T_{\varphi_{\mathbf{m}}}^{\Delta t}$ is a diffeomorphism from $\mathbf{C}$ to $\mathbf{C}'$ and maps each $\mathbf{u} \in \mathbf{C}$ to the $\mathbf{u}' \in \mathbf{C}'$ with the smallest distance to $\mathbf{u}$ where the distance is taken with respect to the spherical geodesics. Now let $\mathbf{u} \in \mathbf{C}$. Then $\mathbf{x} = \mathcal{S}(u)$ is an element of the isophote $\gamma(\mathbf{0})$ passing through the origin. Further let $\mathbf{x}' = T_{\varphi_{\mathbf{m}}}^{\Delta t}(\mathbf{u})$. We are interested in the distance of $\mathbf{x}'$ from the center $\mathbf{m}$ and its dependence on Δt. We investigate how much this distance differs from a linear shift by Δt towards the center $\mathbf{m}$ by defining the error

$$\epsilon = \left| \mathbf{x}' - \left(\mathbf{x} + \Delta t \frac{\mathbf{x} - \mathbf{m}}{|\mathbf{x} - \mathbf{m}|} \right) \right|. \tag{78}$$

The error ϵ is maximized for $\mathbf{x} \in \gamma(\mathbf{0})$ with the largest distance from $\mathbf{0}$, which is $\mathbf{x}_{max} = (2r_{\mathbf{m}}, 0)^T$ with respect to our choice of $\mathbf{m}$, and is minimized for $\mathbf{x}_{min} = \mathbf{0} \in \gamma(\mathbf{0})$. A first order Taylor expansion of T with respect to Δt yields

$$\epsilon_{max} = |T_{\varphi_{\mathbf{m}}}^{\Delta t}(\mathbf{x}_{max}) - (2r_{\mathbf{m}} + \Delta t, 0)^T| \tag{79}$$

$$\approx |\Delta t (2r_{\mathbf{m}}(1 + 4r_{\mathbf{m}}^2)^{\frac{3}{2}} - 1)|, \tag{80}$$

$$\epsilon_{min} = |T_{\varphi_{\mathbf{m}}}^{\Delta t}(\mathbf{x}_{min}) - (\Delta t, 0)^T| \tag{81}$$

$$\approx |\Delta t (3r_{\mathbf{m}}(1 + 4r_{\mathbf{m}}^2)^{-\frac{1}{2}} - 1)|. \tag{82}$$

□

The theorem above tells us, that the approximation of the plane wave is most accurate for points $\mathbf{u} \in \mathbb{S}^2$ located on those circles on $\mathbb{S}^2$, whose characterizing plane intersecting $\mathbb{S}^2$ has a small distance from the origin, which is further illustrated by Fig. 6. Since we embed our projected signal in the Poisson scale space in $\mathbb{R}^4_+$ as $g_{\mathbf{m}}^{\mathbf{x},s}$, the Poisson kernel introduces a high weighting for points on $\mathbb{S}^2$ near the south-pole. This weighting results in high weights for points on planes with small distance to the origin and low weights for planes with high distance to the origin, adjusting for the accuracy of the approximation towards the more accurate regions. The diffusion resulting from the convolution with the Poisson kernel is the standard diffusion on $\mathbb{R}^4_+$ which acts like a low-pass filter on the plane wave ψ_s approximated by $g_{\mathbf{m}}^{\mathbf{x},s}$. The scale s controls the size of the convolution mask pulled back to the plane by the stereographic projection. It is responsible for the accuracy of the plane wave approximation with respect to the radius of the circular signals. For larger radii $r_{\mathbf{m}}$, the window size has to be increased such that the isophote passing through the point of interest is completely projected to $\mathbb{S}^2$. With respect to the original signal $f_{\mathbf{m}}$, the kernels pulled back to the plane do not constitute a linear scale space in the upper half space $\mathbb{R}^3_+$ due to a violation of the semigroup property. Nonetheless with respect to the signal $g_{\mathbf{m}}^{\mathbf{x},s}$ which has been shown to approximate a plane wave in $\mathbb{R}^3$, it constitutes the standard Poisson scale space in the upper half space $\mathbb{R}^4_+$.

3.10 The Conformal Monogenic Signal

We will now use theorem 2 to characterize the behavior of $g_{\mathbf{m}}^{\mathbf{x},s}$ under the Radon transform and the generalized Hilbert transform in $\mathbb{R}^3$. Since the Radon transform integrates over planes in $\mathbb{R}^3$, we know that the Radon transform $\mathcal{R}[g_{\mathbf{m}}^{\mathbf{x},s}](\boldsymbol{\xi}, t)$ will be most accurate for $t \in [-\varepsilon, \varepsilon]$ and ε sufficiently small. This behavior does not interfere with our consideration since we always evaluate the generalized Hilbert transform at the origin which results in an implicit evaluation of the Radon transform at $t = 0$. Due to the additional weighting with a one-dimensional Poisson kernel in the Radon domain along each slice (compare equation (56)), the more inaccurate approximations will be further suppressed. The Radon transform of $g_{\mathbf{m}}^{\mathbf{x},s}$ is, for sufficiently small $t \in [-\varepsilon, \varepsilon]$, $\varepsilon \ll 1$, up to a constant $c' \in \mathbb{R}$ equal to the Radon transform of ψ_s

$$\mathcal{R}[g_{\mathbf{m}}^{\mathbf{x},s}](\boldsymbol{\xi}, t) = c' \mathcal{R}[\psi_s](\boldsymbol{\xi}, t). \tag{83}$$

Since the Radon transform integrates over all hyperplanes in $\mathbb{R}^3$ and $g_{\mathbf{m}}^{\mathbf{x},s}$ is supported on a two-dimensional surface in $\mathbb{R}^3$, namely the sphere $\mathbb{S}^2$, the integration of the Radon transform has to be understood with respect to a certain Radon measure. Let $\mathbf{P}$ denote a plane in $\mathbb{R}^3$ with $\mathbf{C} = \mathbf{P} \cap \mathbb{S}^2$ such that $\mathbf{C} \neq \emptyset$. If we integrate over the plane $\mathbf{P}$, we actually want to integrate $g_{\mathbf{m}}^{\mathbf{x},s}$ over the circle $\mathbf{C}$. Since this is a Lebesgue null set with respect to the standard Lebesgue measure in the plane, we have to introduce an alternate measure. Instead, the Radon transform has to be understood with respect to the Radon measure $\delta(\mathbf{C}(\mathbf{u}))d\mathbf{u}$ where $\mathbf{C}(\mathbf{u}) = 0 \Leftrightarrow \mathbf{u} \in \mathbf{C}$ and δ denotes the Delta distribution (see also [23]). Nonetheless all the above considerations stay valid with respect to this alternate measure. From (83) in conjunction with (56) and (58) we directly conclude that

$$\mathcal{R}^{-1}[\mathcal{R}[\mathcal{H}^i[g_{\mathbf{m}}^{\mathbf{x},s}]]](\mathbf{u}) \tag{84}$$

$$= \mathcal{Q}_s^i[g_{\mathbf{m}}^{\mathbf{x}}](\mathbf{u}) \tag{85}$$

$$= \omega_i \, c' \, \mathcal{R}^{-1}[(\boldsymbol{\xi}, t) \mapsto \mathcal{H}^{1D}[\mathcal{R}[\psi_s](\boldsymbol{\xi}, \cdot)](t)](\mathbf{u}). \tag{86}$$

For a graphical illustration of this important relationship we refer to Fig. 8.

Keeping this relationship in mind, we introduce the conformal monogenic signal as:

Definition 2 (Conformal Monogenic Signal) Let $f_{\mathbf{m}}$ be a curved signal in $\mathbb{R}^2$ and $g_{\mathbf{m}}^{\mathbf{x}}$ its embedding in $\mathbb{R}^3$. Let $\mathcal{H}[\cdot]$ denote the generalized Hilbert transform operator in $\mathbb{R}^3$. Then for $\mathbf{x} \in \mathbb{R}^2$

$$\mathbf{f}(\mathbf{x}) = \begin{pmatrix} g_{\mathbf{m}}^{\mathbf{x}}(\mathbf{0}) \\ \mathcal{H}^1[g_{\mathbf{m}}^{\mathbf{x}}](\mathbf{0}) \\ \mathcal{H}^2[g_{\mathbf{m}}^{\mathbf{x}}](\mathbf{0}) \\ \mathcal{H}^3[g_{\mathbf{m}}^{\mathbf{x}}](\mathbf{0}) \end{pmatrix} = \begin{pmatrix} g_{\mathbf{m}}^{\mathbf{x}}(\mathbf{0}) \\ (h^1 * g_{\mathbf{m}}^{\mathbf{x}})(\mathbf{0}) \\ (h^2 * g_{\mathbf{m}}^{\mathbf{x}})(\mathbf{0}) \\ (h^3 * g_{\mathbf{m}}^{\mathbf{x}})(\mathbf{0}) \end{pmatrix} \tag{87}$$

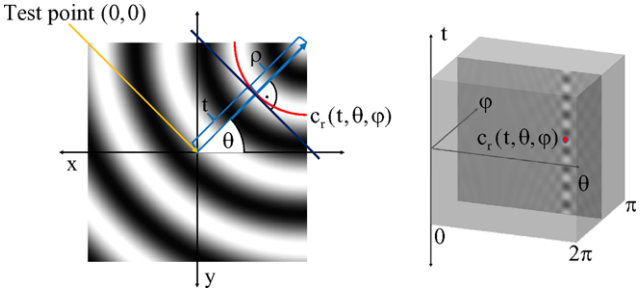

Fig. 8 *Left figure*: Curved i2D signal with direction θ and curvature $\kappa = \frac{1}{\rho}$. *Right figure*: Corresponding 3D Radon space representation of the i2D signal spanned by the parameters t, θ and φ

is called the conformal monogenic signal of $f_{\mathbf{m}}$. Its scale space embedding in the Poisson scale space is obtained by convolution with the Poisson kernel for the upper half space $\mathbb{R}^4_+$ such that

$$\mathbf{f}_s(\mathbf{x}) = \begin{pmatrix} \mathcal{P}_s[g^{\mathbf{x}}_{\mathbf{m}}](\mathbf{0}) \\ \mathcal{Q}^1_s[g^{\mathbf{x}}_{\mathbf{m}}](\mathbf{0}) \\ \mathcal{Q}^2_s[g^{\mathbf{x}}_{\mathbf{m}}](\mathbf{0}) \\ \mathcal{Q}^3_s[g^{\mathbf{x}}_{\mathbf{m}}](\mathbf{0}) \end{pmatrix} = \begin{pmatrix} g^{\mathbf{x},s}_{\mathbf{m}}(\mathbf{0}) \\ \mathcal{H}^1[g^{\mathbf{x},s}_{\mathbf{m}}](\mathbf{0}) \\ \mathcal{H}^2[g^{\mathbf{x},s}_{\mathbf{m}}](\mathbf{0}) \\ \mathcal{H}^3[g^{\mathbf{x},s}_{\mathbf{m}}](\mathbf{0}) \end{pmatrix}. \tag{88}$$

Consider the Radon transform of the partial Hilbert transform in $\mathbb{R}^3$ applied to an embedded curved signal $g^{\mathbf{x},s}_{\mathbf{m}}$ in $\mathbb{R}^3$ with respect to a chosen scale $s \in \mathbb{R}_+$. Its conformal monogenic signal representation in terms of the Radon transform reads

Corollary 4 (Conformal monogenic signal representation of plane waves) *Let* $\mathbf{m} = r_{\mathbf{m}}(\cos(\theta_{\mathbf{m}}), \sin(\theta_{\mathbf{m}}))$, $r_{\mathbf{m}} > 0$, $\varphi_{\mathbf{m}} = \arctan(2r_{\mathbf{m}})$ *and let* $f_{\mathbf{m}}$ *denote a circular signal with center* $\mathbf{m}$. *Then*

$$\mathbf{f}_s(\mathbf{x}) = \begin{pmatrix} \mathcal{P}_s[g^{\mathbf{x}}_{\mathbf{m}}](\mathbf{0}) \\ \mathcal{Q}^1_s[g^{\mathbf{x}}_{\mathbf{m}}](\mathbf{0}) \\ \mathcal{Q}^2_s[g^{\mathbf{x}}_{\mathbf{m}}](\mathbf{0}) \\ \mathcal{Q}^3_s[g^{\mathbf{x}}_{\mathbf{m}}](\mathbf{0}) \end{pmatrix} = \begin{pmatrix} g^{\mathbf{x},s}_{\mathbf{m}}(\mathbf{0}) \\ \sin(\varphi_{\mathbf{m}})\cos(\theta_{\mathbf{m}})\mathcal{T}(\mathbf{0}) \\ \sin(\varphi_{\mathbf{m}})\sin(\theta_{\mathbf{m}})\mathcal{T}(\mathbf{0}) \\ \cos(\varphi_{\mathbf{m}})\mathcal{T}(\mathbf{0}) \end{pmatrix} \tag{89}$$

with

$$\mathcal{T}(\mathbf{u}) = c'\mathcal{R}^{-1}[(\boldsymbol{\xi}, t) \mapsto \mathcal{H}^{1D}[\mathcal{R}[g^{\mathbf{x},s}_{\mathbf{m}}](\boldsymbol{\xi}, \cdot)](t)](\mathbf{u}) \tag{90}$$

and $c' \in \mathbb{R}$.

Proof Let $\mathbf{x} \in \mathbb{R}^2$. Then with respect to $\mathbf{x}$, $g^{\mathbf{x},s}_{\mathbf{m}}$ approximates the plane wave ψ_s in $\mathbb{R}^3$ with orientation vector

$$\begin{aligned} \boldsymbol{\omega} &= (\sin(\varphi_{\mathbf{m}})\cos(\theta_{\mathbf{m}}), \sin(\varphi_{\mathbf{m}})\sin(\theta_{\mathbf{m}}), \cos(\varphi_{\mathbf{m}}))^T \\ &= \left(\frac{1}{4} + r^2_{\mathbf{m}}\right)^{-\frac{1}{2}} \left(r_{\mathbf{m}}\cos(\theta_{\mathbf{m}}), r_{\mathbf{m}}\sin(\theta_{\mathbf{m}}), \frac{1}{2}\right)^T \end{aligned} \tag{91}$$

according to Theorem 2. Applying (84) to the components of the conformal monogenic signal concludes the proof. □

We are now able to relate the orientation vector of the plane wave approximated by $g^{\mathbf{x},s}_{\mathbf{m}}$ to the normal vector of the plane intersecting $\mathbb{S}^2$, which contains the isophote passing through $\mathbf{x}$:

Corollary 5 (Isophote-Plane-Wave relationship) *Let* $\mathbf{m} = r_{\mathbf{m}}(\cos\theta_{\mathbf{m}}, \sin\theta_{\mathbf{m}})$, $r_{\mathbf{m}} > 0$ *and let* $f_{\mathbf{m}}(\mathbf{x}) = a\cos(k|\mathbf{m} - \mathbf{x}| + \phi)$ *denote a circular signal with center* $\mathbf{m}$, *amplitude* $a \in \mathbb{R}$, *linear phase* $\phi \in [0, 2\pi]$ *and frequency* $k \in \mathbb{R}_+$. *Fix* $\mathbf{x} \in \mathbb{R}^2$. *Let* $g^{\mathbf{x},s}_{\mathbf{m}}$ *be the embedding of* $f_{\mathbf{m}}$ *with respect to* $\mathbf{x}$. *Further let* $\psi(\mathbf{u}) = a\cos(k\langle \mathbf{u}, \boldsymbol{\omega}\rangle + k\, r_{\mathbf{m}} + \phi)$ *denote the plane wave in* $\mathbb{R}^3$ *with orientation vector*

$$\begin{aligned} \boldsymbol{\omega} &= (\sin(\varphi_{\mathbf{m}})\cos(\theta_{\mathbf{m}}), \sin(\varphi_{\mathbf{m}})\sin(\theta_{\mathbf{m}}), \cos(\varphi_{\mathbf{m}}))^T \\ &= \left(\frac{1}{4} + r^2_{\mathbf{m}}\right)^{-\frac{1}{2}} \left(r_{\mathbf{m}}\cos(\theta_{\mathbf{m}}), r_{\mathbf{m}}\sin(\theta_{\mathbf{m}}), \frac{1}{2}\right)^T \end{aligned} \tag{92}$$

and scale space embedding ψ_s. *Denote by* $\gamma_{\mathbf{m}}(\mathbf{x})$ *the isophote of the function* $f_{\mathbf{m}}$ *passing through our point of interest* $\mathbf{x} \in \mathbb{R}^2$. *Further let* $\mathbf{n}_{\mathbf{m}}$ *denote the normal vector of the plane* $\mathbf{P}_{\mathbf{m}}$ *with*

$$\mathbf{P}_{\mathbf{m}} \cap \mathbb{S}^2 = \{\mathcal{S}^{-1}(\mathbf{y}) : \mathbf{y} \in \gamma_{\mathbf{m}}(\mathbf{x})\}. \tag{93}$$

Then it holds that

$$\mathbf{n}_{\mathbf{m}} = \boldsymbol{\omega}. \tag{94}$$

Proof According to Theorem 2, $g^{\mathbf{x},s}_{\mathbf{m}}$ approximates ψ_s whose orientation vector is $\boldsymbol{\omega}$. But according to Theorem 1, $\boldsymbol{\omega}$ is exactly the normal vector of $\mathbf{P}_{\mathbf{m}}$. □

We are now able to estimate the normal vector $\mathbf{n}_{\mathbf{m}}$ by estimating the orientation vector $\boldsymbol{\omega}$ of the corresponding plane ψ_s wave approximated by $g^{\mathbf{x},s}_{\mathbf{m}}$. The estimates are obtained from the conformal monogenic signal representation of $g^{\mathbf{x},s}_{\mathbf{m}}$ using Corollaries 4 and 5 as:

$$\theta_{\mathbf{m}}(\mathbf{x}) = \arctan 2\left(\mathcal{Q}^2_s[g^{\mathbf{x}}_{\mathbf{m}}](\mathbf{0}), \mathcal{Q}^1_s[g^{\mathbf{x}}_{\mathbf{m}}](\mathbf{0})\right) \tag{95}$$

and

$$\varphi_{\mathbf{m}}(\mathbf{x}) = \arctan\left(\frac{\sqrt{\mathcal{Q}^1_s[g^{\mathbf{x}}_{\mathbf{m}}](\mathbf{0})^2 + \mathcal{Q}^2_s[g^{\mathbf{x}}_{\mathbf{m}}](\mathbf{0})^2}}{\mathcal{Q}^3_s[g^{\mathbf{x}}_{\mathbf{m}}](\mathbf{0})}\right) \tag{96}$$

such that the curvature of the isophote passing through $\mathbf{x}$ is obtained as

$$\kappa_{\mathbf{m}}(\mathbf{x}) = \frac{2}{\tan(\varphi_{\mathbf{m}}(\mathbf{x}))} = \frac{2\mathcal{Q}^3_s[g^{\mathbf{x}}_{\mathbf{m}}](\mathbf{0})}{\sqrt{\mathcal{Q}^1_s[g^{\mathbf{x}}_{\mathbf{m}}](\mathbf{0})^2 + \mathcal{Q}^2_s[g^{\mathbf{x}}_{\mathbf{m}}](\mathbf{0})^2}}. \tag{97}$$

The parameter $\theta_{\mathbf{m}}$ will be interpreted as the orientation $\theta \in [0, \pi)$ in i1D case and naturally deploys to direction $\theta \in [0, 2\pi)$ for the i2D case. In Sect. 3.7 we have already classified single isophotes into straight lines and curved isophotes depending on the angle $\varphi_{\mathbf{m}}$. Since we have now established the link between single isophotes and curved signals, we are able to classify the underlying signal type. Figure 9 illustrates, that we are able to distinguish i1D and curved i2D signals, depending on the angle $\varphi_{\mathbf{m}}$. As $\varphi_{\mathbf{m}}$ approaches $\frac{\pi}{2}$, a i1D signal is approximated. Otherwise the underlying signal is a curved i2D signal. Consequently the conformal monogenic signal is able to estimate the intrinsic dimension of the underlying signal. Further, the local amplitude of the conformal monogenic signal $\mathbf{f}_s$ is defined by

$$a_{\mathbf{m}}(\mathbf{x}) = \sqrt{\mathcal{P}_s[g^{\mathbf{x}}_{\mathbf{m}}](\mathbf{0})^2 + \sum_{i=1}^{3} (\mathcal{Q}^i_s[g^{\mathbf{x}}_{\mathbf{m}}](\mathbf{0}))^2}. \tag{98}$$

The i1D and i2D phase of curved 2D signals is defined by

$$\phi_{\mathbf{m}}(\mathbf{x}) = \arctan 2 \left(\sqrt{\sum_{i=1}^{3} (\mathcal{Q}^i_s[g^{\mathbf{x}}_{\mathbf{m}}](\mathbf{0}))^2}, \mathcal{P}_s[g^{\mathbf{x}}_{\mathbf{m}}](\mathbf{0}) \right) \tag{99}$$

where the phase indicates a measure of parity symmetry as it is known from classical phase based signal analysis. It is worth noting that all these properties have been obtained by the conformal monogenic signal filterset in (88) which is based on simple convolutions with the Poisson kernel and its conjugate parts. The linear shift invariance and the rotational equivariance of the generalized Hilbert transform carry over to the conformal monogenic signal. It follows that the properties phase, curvature and direction are invariant with respect to constant illumination changes. Figures 10 and 11 show the features of the conformal monogenic signal obtained from two synthetic signals. We notice that the phase and the orientation are exactly the features which can be obtained from the classical monogenic signal. But in addition we also obtain the isophote curvature of the input signal. Note that the curvature information may serve as a corner measure as indicated in the figure the output to a classical Sobel edge detector.

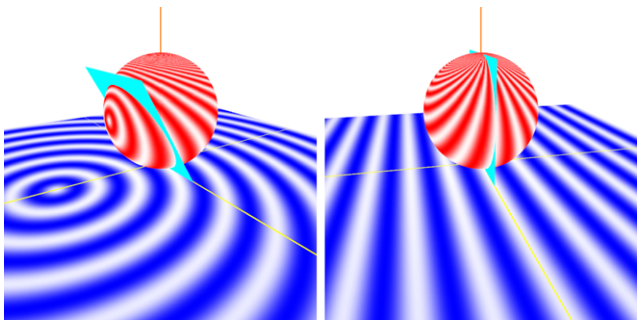

Fig. 9 *Left figure*: The plane indicates an i2D signal. *Right figure*: The plane of an i1D signal passes through the north pole of the sphere

4 Experiments

We are interested in the accuracy of our curvature estimator. Since experiments regarding the orientation and the phase of the monogenic signal have already been carried out in the mentioned literature, we focus on experiments concerning the new curvature feature.

4.1 Planar Curves

We first evaluate the proposed method for planar curves. Let $\mathbf{l}(t) = (x(t), y(t))$, $t \in [a, b]$ be a part of a parameterized plane curve. Then we sample $\mathbf{l}$ as $\mathbf{l}_i = (x(i\,d), y(i\,d))$, $i \in$

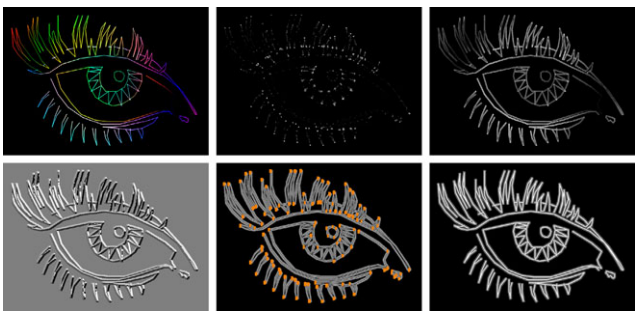

Fig. 11 *Top row* from left to right: Original signal, isophote curvature [12] and Sobel detector output. *Bottom row* from left to right: *Conformal monogenic signal* direction, curvature and phase. Note the observable illumination invariance of the conformal curvature and phase. Convolution mask size: 7×7 pixels

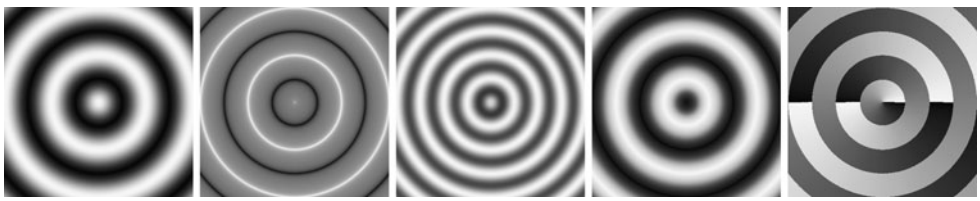

Fig. 10 From left to right: Original synthetic i2D signal $f(\mathbf{x}) = a_0 \cos(\sqrt{x_1^2 + x_2^2})$, *conformal monogenic signal* curvature, *conformal monogenic signal* amplitude, phase and direction. Convolution mask size: 11×11 pixels. Rotational invariance and isotropic properties can be clearly seen

$\{1,\ldots,N\}, d=\frac{|a-b|}{N}, N\in\mathbb{N}$. The estimation of the curvature relies on the choice of a scale described by the neighborhood or window size $W\in\mathbb{N}$ with respect to the current point of interest. For each point $\mathbf{l}_i$ we first shift the neighborhood $NB_W(\mathbf{l}_i)=\{\mathbf{l}_{i-W},\ldots,\mathbf{l}_i,\ldots,\mathbf{l}_{i+W}\}$ to the origin and project it to the sphere $\mathbb{S}^2$ such that $NB'_W(\mathbf{l}_i)=\{\mathcal{S}^{-1}(\mathbf{l}_{i-W}-\mathbf{l}_i),\ \ldots,(0,0,0),\ldots,\mathcal{S}^{-1}(\mathbf{l}_{i+W}-\mathbf{l}_i)\}$. The curvature is then obtained as

$$\kappa_W(\mathbf{l}_i)=2\frac{M_W^3}{((M_W^1)^2+(M_W^2)^2)^{(1/2)}} \tag{100}$$

with

$$M_W^k=\sum_{j=-W}^{W} q_W^k(\mathcal{S}^{-1}(\mathbf{l}_{i+j}-\mathbf{l}_i)),\quad k\in\{1,2,3\} \tag{101}$$

where q_W^k denotes the k-th component of the conjugate Poisson kernel in the upper half space $\mathbb{R}^4_+$ with respect the scale W. We compare our method to curvature estimations obtained by circle fittings through the points of the neighborhood $NB'_W(\mathbf{l}_i)$. To fit a circle through these points we use two different distance functions which are minimized, an algebraic distance according to [9] and a geometric distance according to [2].

Algebraically a circle may be represented as the set of all $\mathbf{x}\in\mathbb{R}^2$ satisfying

$$a\mathbf{x}^T\mathbf{x}+\mathbf{b}^T\mathbf{x}+c=0 \tag{102}$$

with $a\neq 0, \mathbf{b}\in\mathbb{R}^2, c\in\mathbb{R}$. We fit a circle through the points $\mathbf{x}\in NB(\mathbf{l}_i,W)$ by minimizing

$$\|A\mathbf{u}\|=\min\quad \text{s.t.}\quad \|\mathbf{u}\|=1 \tag{103}$$

with

$$A=\begin{pmatrix} x_{11}^2+x_{12}^2 & x_{11} & x_{12} & 1\\ \vdots & \vdots & \vdots & \vdots\\ x_{m1}^2+x_{m2}^2 & x_{m1} & x_{m2} & 1\end{pmatrix} \tag{104}$$

and $m=2W+1, \mathbf{u}=(a,b_1,b_2,c)^T$. The radius of curvature r is then obtained as

$$r=\sqrt{\frac{\sqrt{b_1^2+b_2^2}}{4a^2}-\frac{c}{a}}. \tag{105}$$

The second method, which we refer to as the geometric method, minimizes the distance

$$\sum_{j=1}^{2W+1}(x_{j1}-a_1)^2+(x_{j2}-a_2)^2-r^2 \tag{106}$$

which is minimized for the unknown center $\mathbf{a}=(a_1,a_2)\in\mathbb{R}^2$ and the unknown radius r by solving a linear least-squares problem (see [2]). The radius serves as a curvature measure due to the already mentioned relation $\kappa=\frac{1}{r}$. Figure 12 shows the comparison of our method with the algebraic and geometric fitting method for three test curves with and without noise. We measured the absolute average error over all curve points for different window sizes as

$$E_W(\mathbf{l})=\sum_{i=1}^{|\mathbf{l}|}|\kappa(\mathbf{l}_i)-\tilde{\kappa}_W(\mathbf{l}_i)| \tag{107}$$

where $\kappa(\mathbf{l}_i)$ denotes the ground truth curvature and $\tilde{\kappa}_W(\mathbf{l}_i)$ the estimated curvature of the curve at $\mathbf{l}_i$. It turns out that our novel method converges to the true radius of curvature in the case of the assumed signal model, a circle. Compared to the two methods based on circle fittings, it is robust against noise resulting in accurate curvature estimations. Note that the figure depicts the average error over all curve points depending on the window size. Since the curvature is not constant for all curve points in the case of the ellipse and the spiral there are always points on the curve for which the given window size provides a correct estimate but also points for which the given window size provides incorrect results, affecting the overall average error. Therefore there is no convergent behaviour with respect to the average error for these curve types. But actually this is also a problem of the estimators we compared our method to, so you notice that our estimator behaves like the standard estimators and delivers comparable results.

4.2 Digital Images

The curvature estimation based on the conformal monogenic signal has the advantage, that it is not limited to digital curves but can also be applied to images, where the curves are not known in advance, e.g. isophotes in gray-scale images. In these cases the curvature is often supposed to serve as a feature indicating corners or straight line segments in the case of high or low curvature. The standard method to obtain the isophote curvature in digital images uses first and second order derivatives. To be comparable to our method, which we introduced in a scale space embedding, we introduce the classical derivative based method to calculate the isophote curvature as [15]

$$\kappa=\frac{2G_{1,0}^{s_1,s_2}G_{0,1}^{s_1,s_2}G_{1,1}^{s_1,s_2}-(G_{1,0}^{s_1,s_2})^2G_{0,2}^{s_1,s_2}-(G_{0,1}^{s_1,s_2})^2G_{2,0}^{s_1,s_2}}{((G_{1,0}^{s_1,s_2})^2+(G_{0,1}^{s_1,s_2})^2)^{3/2}} \tag{108}$$

where $G_{i,j}^{s_1,s_2}$ denotes the convolution with the i-th and j-th order derivatives of Difference-Of-Gaussian kernels with

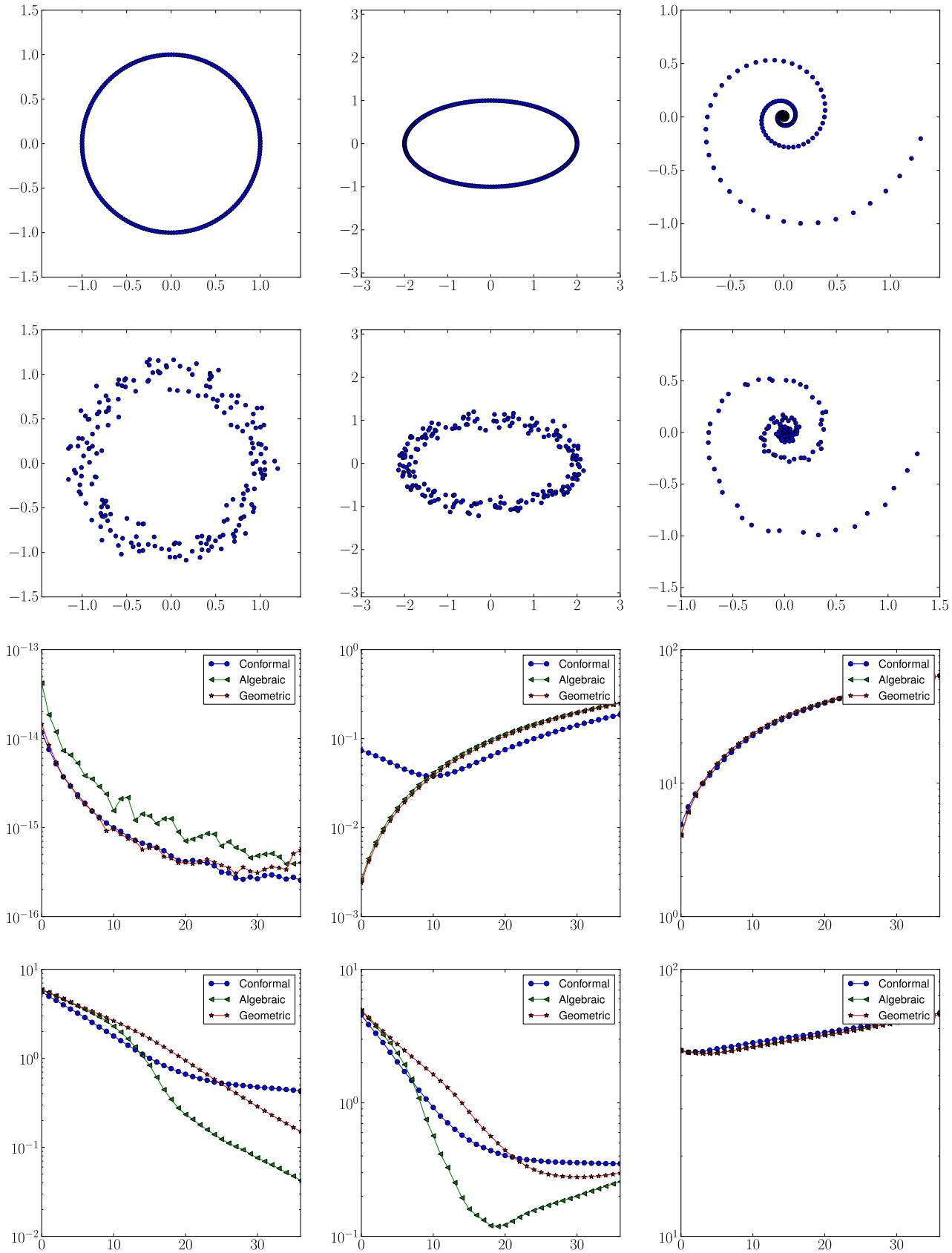

Fig. 12 *First row*: Test curves sampled at 200 points. *Second row*: Gaussian white noise perturbed test curves, $\sigma = 0.1$. *Third* and *fourth row*: Average absolute curvature errors E_W over all curve points depending on the window size W (abscissa) without and with noise (see also (107))

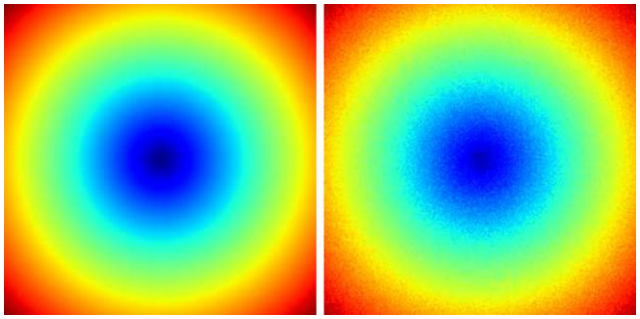

Fig. 13 *Left*: Ground truth image $f(\mathbf{x}) = \sqrt{x_1^2 + x_2^2}$. *Right*: Ground truth image perturbed with Gaussian white noise, $\sigma = 0.1$

scales s_1, s_2 along the x_1 and x_2 axes. To study the accuracy of our estimator we apply it to the artificial signal $f(\mathbf{x}) = \sqrt{x_1^2 + x_2^2}$. Since the test signal depends linearly on the distance from the origin, its ground truth isophote curvature reads $\kappa(\mathbf{x}) = (x_1^2 + x_2^2)^{(-1/2)}$. Figure 13 shows the test signal with and without noise. In Fig. 14 the curvature obtained for different scales is plotted against the ground truth curvature. The left column shows the results obtained from the conformal monogenic signal. The right column shows the results obtained from (108). Since the ground truth signal is isotropic, the plot is restricted to the slice $(x_1, 0)$. Figure 15 depicts the same situation but with respect to the noise perturbed ground truth image. With increasing convolution mask size the accuracy of our proposed estimator increases and finally converges to the true curvature. Further it performs better than the derivative based method on the noise perturbed signal, especially for small convolution mask sizes. Figure 16 shows the average absolute error of the curvature over the whole image for the conformal and the derivative based method. Again the noiseless and the noise perturbed case are shown. It justifies our proposed method as a robust and accurate curvature estimator.

Another important aspect of the isophote curvature information is the ability to obtain the ridge curves of an image [15]. The ridge curves are the isophotes for which the gradient vanishes such that the curvature obtained by (108) is degenerate. Due to their invariance properties concerning translation, rotation and monotonic intensity changes, ridges serve as a useful feature, especially if their evolution is considered across multiple scales. Figure 17 shows the ridge curves (degeneracies of the isophote curvature) of the Lenna test-image obtained by the proposed method using (97) and the curvature obtained according to the classical (108) using Difference-of-Gaussian convolutions kernels across different scales. Based on the results we conclude that our proposed estimator delivers results comparable to the standard method and therefore provides practical alternative access to the problem of isophote curvature estimation.

5 Outlook: The 3D Conformal Monogenic Signal

While the last chapter focused on the analysis of curved signal structures in the Euclidean plane using the conformal monogenic signal, this section is supposed to provide an outlook on how the proposed signal model can be generalized to three dimensions. It serves as a novel tool for volume and image-sequence processing.

Analogous to the previous chapters our signal model are signals

$$f_{\mathbf{m}}(\mathbf{x}) = a\cos(k\,|\mathbf{x} - \mathbf{m}| + \phi) \tag{109}$$

with $\mathbf{x}, \mathbf{m} \in \mathbb{R}^3, a \in \mathbb{R}, k \in \mathbb{R}_+, \phi \in [0, 2\pi]$

$$\mathbf{m} = \begin{pmatrix} m_1 \\ m_2 \\ m_3 \end{pmatrix} = r_{\mathbf{m}} \begin{pmatrix} \sin(\theta_{\mathbf{m},1})\cos(\theta_{\mathbf{m},2}) \\ \sin(\theta_{\mathbf{m},1})\sin(\theta_{\mathbf{m},2}) \\ \cos(\theta_{\mathbf{m},2}) \end{pmatrix} \tag{110}$$

which are spherical signals only depending on the distance from $\mathbf{x}$ to $\mathbf{m}$. In contrast to the two dimensional case, the isophotes $\gamma_{\mathbf{m}}(\mathbf{x})$ of these signals are constituted by spheres in $\mathbb{R}^3$ around $\mathbf{m}$. In order to apply concepts from the previous chapter we project our 3D signal to the hypersphere

$$\mathbb{S}^3 = \left\{ \mathbf{u} \in \mathbb{R}^4 \;\middle|\; \sum_{i=1}^{3} u_i^2 + \left(u_4 - \frac{1}{2}\right)^2 = \left(\frac{1}{2}\right)^2 \right\} \tag{111}$$

using the inverse stereographic projection $\mathcal{S}^{-1} : \mathbb{R}^3 \to \mathbb{S}^3$ given by

$$\mathcal{S}^{-1}(\mathbf{x}) = \frac{1}{1 + \sum_{i=1}^{3} x_i^2} \begin{pmatrix} x_1 \\ x_2 \\ x_3 \\ \sum_{\imath=1}^{3} x_i^2 \end{pmatrix} \tag{112}$$

for $\mathbf{x} \in \mathbb{R}^3$. The projected signal with respect to a point of interest $\mathbf{x} \in \mathbb{R}^3$ is interpreted as a signal $g_{\mathbf{m}} \in L^2(\mathbb{R}^4)$ such that

$$g_{\mathbf{m}}^{\mathbf{x}}(\mathbf{u}) = \begin{cases} f_{\mathbf{m}}(\mathcal{S}(\mathbf{u}) + \mathbf{x}), & \text{if } \mathbf{u} \in \mathbb{S}^3, \\ 0, & \text{else}, \end{cases} \tag{113}$$

where $\mathcal{S}$ denotes the stereographic projection from $\mathbb{S}^3$ to $\mathbb{R}^3$. The standard three dimensional monogenic signal is able to obtain the local orientation, local phase and local amplitude of plane waves in $\mathbb{R}^3$ given by

$$f(\mathbf{x}) = a\cos(k\,\langle \boldsymbol{\omega}, \mathbf{x} \rangle + \phi) \tag{114}$$

where $\boldsymbol{\omega} \in \mathbb{R}^3, |\boldsymbol{\omega}| = 1$ denotes the orientation of the plane wave, ϕ the phase and a the amplitude.

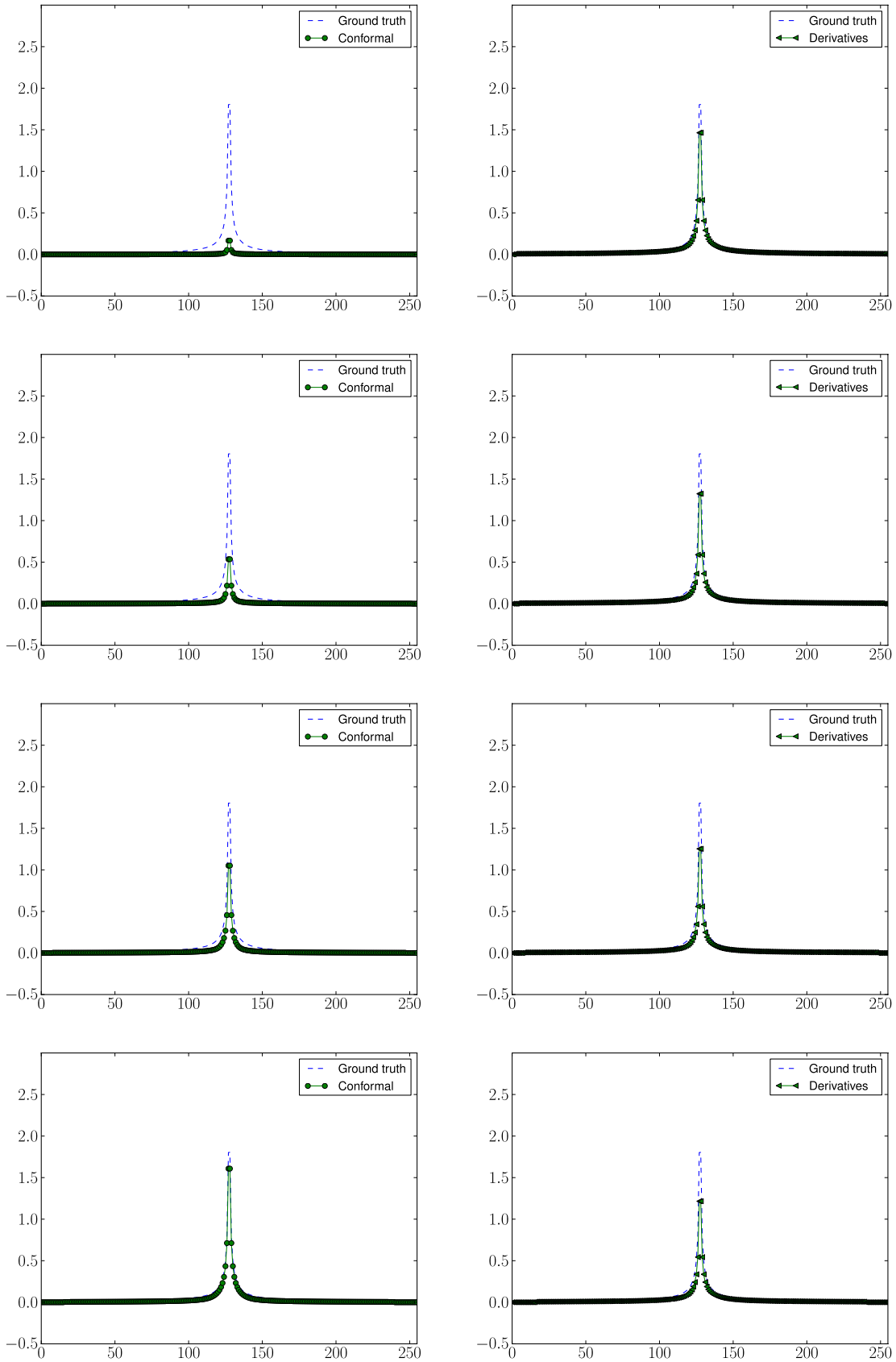

Fig. 14 Estimated curvatures of the ground truth image without noise for the slice $f(x_1, 0)$ and scales $(s_1, s_2) \in \{(1, 2), (2, 4), (4, 8), (8, 16)\}$ (from top to bottom). *Left column*: Conformal method. *Right column*: Derivative based method

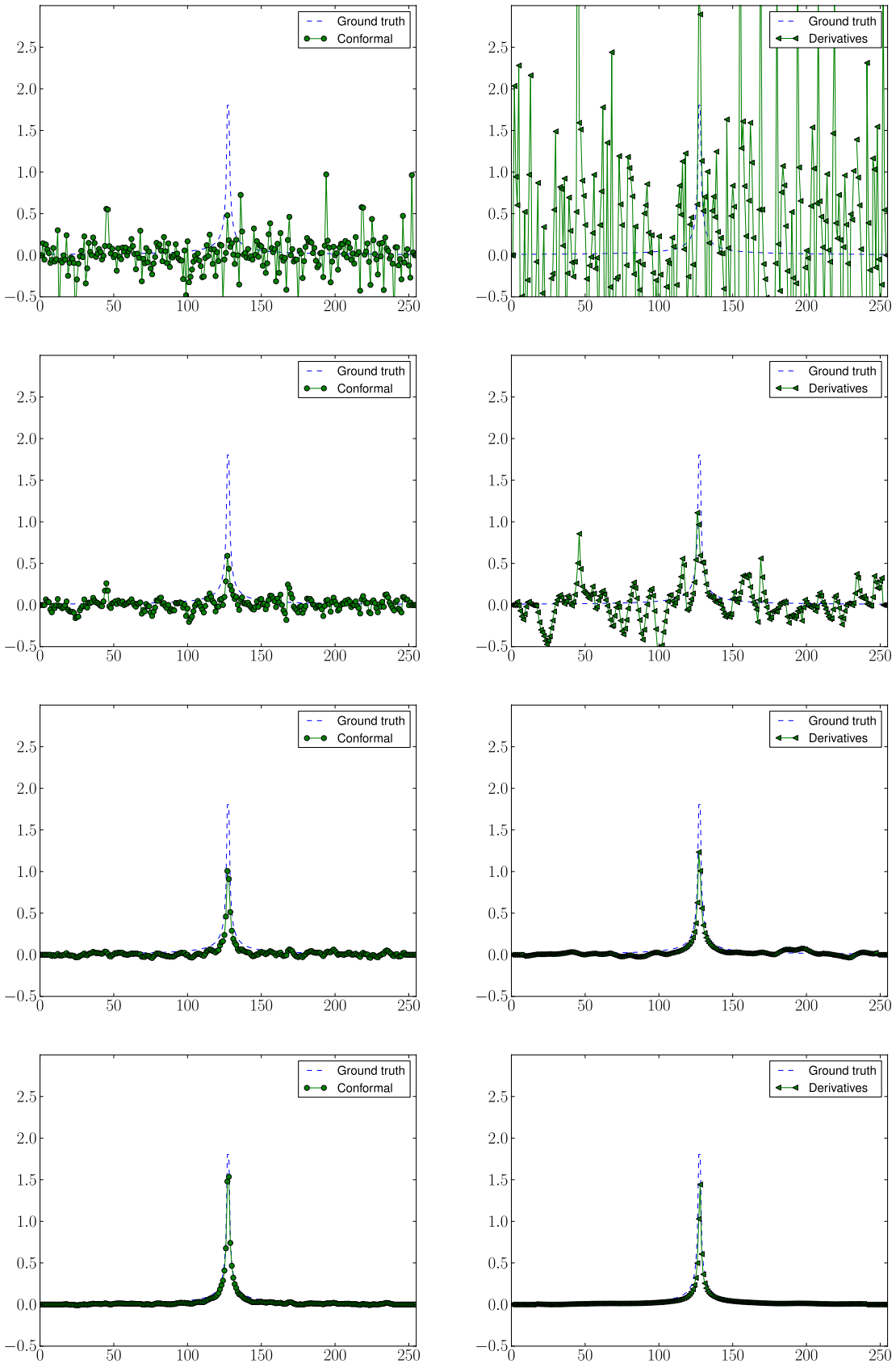

Fig. 15 Estimated curvatures of the ground truth image with noise for the slice $f(x_1, 0)$ and scales $(s_1, s_2) \in \{(1, 2), (2, 4), (4, 8), (8, 16)\}$ (from top to bottom). *Left column*: Conformal method. *Right column*: Derivative based method

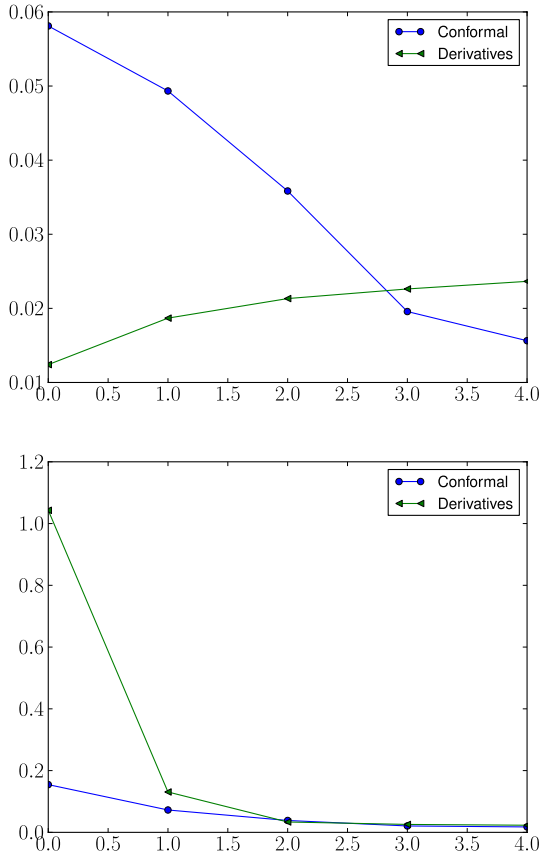

Fig. 16 Average absolute curvature errors for our ground truth signals in Fig. 13 (*top*: no noise, *bottom*: noise perturbed) over the whole images for scales $(s_1, s_2) = (2^x, 2^{x+1})$ calculated for the conformal and the derivative based method, where x is the abscissa

In analogue to the two-dimensional case, the conformal monogenic signal is supposed to extend the monogenic signal such that curved signal structures, in this case spherical signal structures, can by analyzed. The type of curved signals which can be analyzed is again determined by the geometric entities represented by the intersection of hyperplanes with the sphere. Compared to the two-dimensional case the hyperplanes are now three-dimensional. While the intersections of planes and $\mathbb{S}^2$ were circles in the two-dimensional case, we now deal with spheres contained in the surface of the hypersphere $\mathbb{S}^3$ passing through the south-pole of $\mathbb{S}^3$. Since we chose $\mathbb{S}^3$ such that its south-pole coincides with the origin of $\mathbb{R}^4$, these hyperplanes pass through the origin in $\mathbb{R}^4$. We are therefore able to characterize these hyperplanes by just using their normal vectors.

We consider the Radon transform in $\mathbb{R}^4$, which integrates over 3 dimensional hyperplanes in $\mathbb{R}^4$. Using the relationship between the Radon transform in $\mathbb{R}^4$ and the generalized Hilbert transform in $\mathbb{R}^4$ in analogue to the relationship in $\mathbb{R}^3$, we notice that for a projected spherical signal $g_{\mathbf{m}}^{\mathbf{x},s}$ with respect to a point of interest $\mathbf{x} \in \mathbb{R}^3$ and scale $s \in \mathbb{R}_+$, its conformal monogenic signal representation in the Poisson scale-space in the upper half-space $\mathbb{R}^5_+$ reads

$$\mathbf{f}_s(\mathbf{x}) = \begin{pmatrix} \mathcal{P}_s[g_{\mathbf{m}}^{\mathbf{x}}](\mathbf{0}) \\ \mathcal{Q}_s^1[g_{\mathbf{m}}^{\mathbf{x}}](\mathbf{0}) \\ \mathcal{Q}_s^2[g_{\mathbf{m}}^{\mathbf{x}}](\mathbf{0}) \\ \mathcal{Q}_s^3[g_{\mathbf{m}}^{\mathbf{x}}](\mathbf{0}) \\ \mathcal{Q}_s^4[g_{\mathbf{m}}^{\mathbf{x}}](\mathbf{0}) \end{pmatrix} \tag{115}$$

$$= \begin{pmatrix} g_{\mathbf{m}}^{\mathbf{x},s}(\mathbf{0}) \\ \sin(\varphi_{\mathbf{m}})\sin(\theta_{\mathbf{m},2})\cos(\theta_{\mathbf{m},1})\mathcal{T}(\mathbf{0}) \\ \sin(\varphi_{\mathbf{m}})\sin(\theta_{\mathbf{m},2})\sin(\theta_{\mathbf{m},1})\mathcal{T}(\mathbf{0}) \\ \sin(\varphi_{\mathbf{m}})\cos(\theta_{\mathbf{m},2})\mathcal{T}(\mathbf{0}) \\ \cos(\varphi_{\mathbf{m}})\mathcal{T}(\mathbf{0}) \end{pmatrix} \tag{116}$$

where

$$\mathcal{T}(\mathbf{u}) = c'\mathcal{R}^{-1}[(\boldsymbol{\xi}, t) \mapsto \mathcal{H}^{1D}[\mathcal{R}[g_{\mathbf{m}}^{\mathbf{x},s}](\boldsymbol{\xi}, \cdot)](t)](\mathbf{u}), \tag{117}$$

with $c' \in \mathbb{R}$.

We are therefore able to extract the direction angles of the original signal $f_{\mathbf{m}}$ in the three-dimensional space at $\mathbf{x} \in \mathbb{R}^3$ as

$$\theta_{\mathbf{m},1}(\mathbf{x}) = \arctan\left(\frac{\mathcal{Q}_s^2[g_{\mathbf{m}}^{\mathbf{x}}](\mathbf{0})}{\mathcal{Q}_s^1[g_{\mathbf{m}}^{\mathbf{x}}](\mathbf{0})}\right), \tag{118}$$

$$\theta_{\mathbf{m},2}(\mathbf{x}) = \arctan 2\left(\sqrt{\mathcal{Q}_s^1[g_{\mathbf{m}}^{\mathbf{x}}](\mathbf{0})^2 + \mathcal{Q}_s^2[g_{\mathbf{m}}^{\mathbf{x}}](\mathbf{0})^2}, \mathcal{Q}_s^3[g_{\mathbf{m}}^{\mathbf{x}}](\mathbf{0})\right). \tag{119}$$

The curvature measure which corresponds to the radius of the spherical signal is obtained as

$$\kappa_{\mathbf{m}}(\mathbf{x}) = \frac{2\mathcal{Q}_s^4[g_{\mathbf{m}}^{\mathbf{x}}](\mathbf{0})}{\sqrt{\sum_{i=1}^3 \mathcal{Q}_s^i[g_{\mathbf{m}}^{\mathbf{x}}](\mathbf{0})^2}} = \frac{2}{\tan\varphi_{\mathbf{m}}(\mathbf{x})}. \tag{120}$$

The amplitude and phase are determined by

$$a(\mathbf{x}) = \sqrt{\mathcal{P}_s[g_{\mathbf{m}}^{\mathbf{x}}](\mathbf{0})^2 + \sum_{i=1}^4 \mathcal{Q}_s^i[g_{\mathbf{m}}^{\mathbf{x}}](\mathbf{0})^2}, \tag{121}$$

$$\phi(\mathbf{x}) = \arctan\frac{\sqrt{\sum_{i=1}^4 \mathcal{Q}_s^i[g_{\mathbf{m}}^{\mathbf{x}}](\mathbf{0})^2}}{\mathcal{P}_s[g_{\mathbf{m}}^{\mathbf{x}}](\mathbf{0})}. \tag{122}$$

The isophote curvature in the three dimensional case represents the curvature of the sphere locally approximating the signal at $\mathbf{x}$. Therefore, we are able to extract the curvature information for all surfaces which may locally be approximated by a sphere.

The conformal monogenic signal in $\mathbb{R}^3$ turns out to be useful in the analysis of volume images. Figure 18 shows

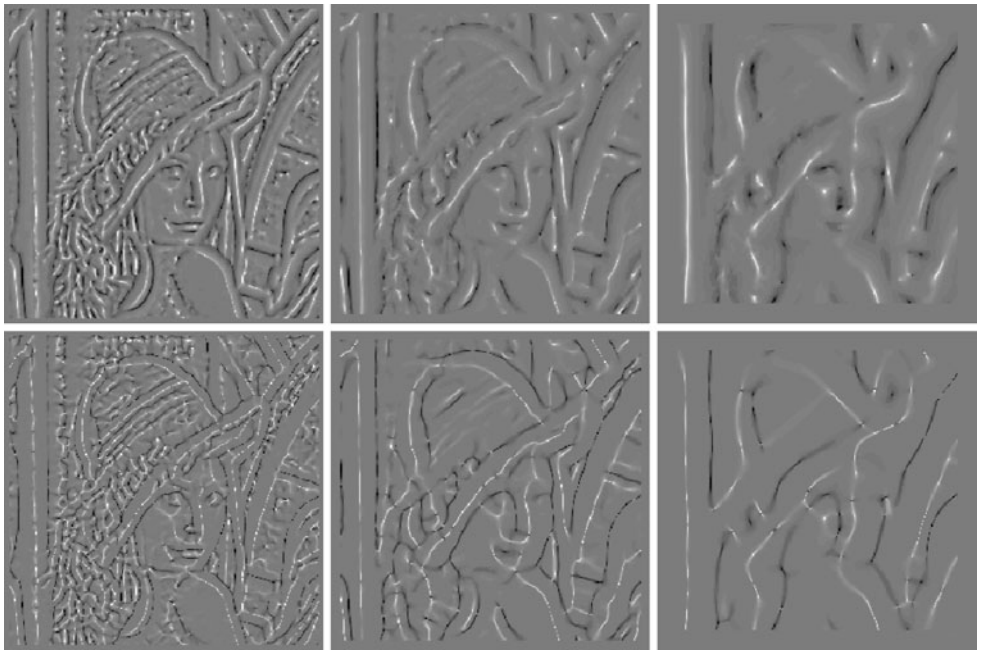

Fig. 17 *Top row*: Isophote curvatures calculated with the proposed method in (97) at scales $(s_1, s_2) = (2, 4), (4, 8), (8, 16)$. *Bottom row*: Isophote curvatures calculated with the classical method in (108) at scales $(s_1, s_2) = (2, 4), (4, 8), (8, 16)$

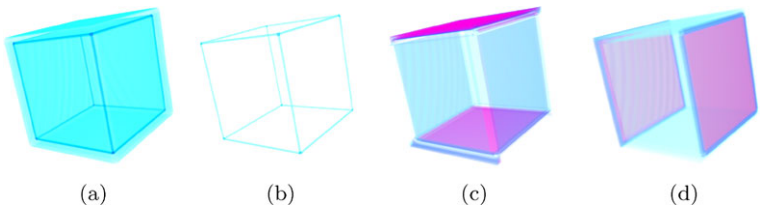

Fig. 18 From left to right: Volume rendering of a cube. (**a**) Regions with low curvature (high radius of curvature). (**b**) Regions with hight curvature (low radius of curvature). (**c**) Direction with respect to $\theta_{\mathbf{m},2}$. (**d**) Direction with respect to $\theta_{\mathbf{m},1}$

Fig. 19 The 3D conformal signal delivers four local features which can be used for image sequence analysis such as optical flow and motion analysis. From left to right: Curvature, phase and the two parts of the direction information. 3D convolution mask size $5 \times 5 \times 5$ pixels

the features of sample volume rendering of a cube. Image (a) shows the regions of the volume rendering where the curvature is low. These are planar regions, since planes correspond to spheres with infinity radius of curvature. Due to the relation $\kappa = \frac{1}{r}$ it follows that the curvature of a plane tends to 0. This can be considered as the analogue to the two-dimensional case, where straight lines represent circles with infinite radius. Image (b) shows the regions with high curvature, which are regions which can be approximated by spheres with low radius. In general this measure of curvature allows us to distinguish between planar surfaces, edges and corners in three-dimensional images. Furthermore, as shown in Figs. 18 (c) and (d), we are able to obtain the direction of these structures with respect to the angles $\theta_{\mathbf{m},1}, \theta_{\mathbf{m},2}$.

The feature set of the conformal monogenic signal in $\mathbb{R}^3$ is not limited to volume images but may also be used for image-sequence analysis. Figure 19 shows the output of the features for frame inside the Yosemite image sequence.

Future work includes the application of the conformal monogenic signal to volume-images as well as image sequences. In volume image processing they may be used for preprocessing, feature detection and image registration. Possible applications in the field of image sequence analysis include the application of the conformal monogenic signal as optical flow constraints.

6 Conclusion

In this contribution a new fundamental idea for locally analyzing curved and straight signals in one unified framework has been presented. It has been shown that the feature space of generalized Hilbert transforms in Euclidean space is too flat for analyzing curved signals. Generalized Hilbert transforms in Euclidean space lack from the restriction to the classical intrinsically 1D local phase information for all signal dimensions. In such a case arbitrary signals can be modeled by a superposition of individual i1D signals. The two-dimensional generalized Hilbert transforms of any order are always limited to the related 2D Radon space which gives direct access to the feature space by formulating explicit systems of equations. The problem of analyzing both i1D and i2D signals in one framework can be solved by embedding n-dimensional signals in $(n+1)$-dimensional conformal spaces in which $(n+1)$-dimensional generalized Hilbert transforms are possible with more degrees of freedom. Without steering and in a rotational invariant way, local signal features such as local amplitude, phase, orientation/direction and curvature can be determined in spatial domain by convolution. The *conformal monogenic signal* can be computed efficiently and can be easily implemented into existing low level signal processing steps of any application. Furthermore, exact curvature can be calculated with all the advantages of rotational invariant local phase based approaches (robustness against local and global signal amplitude changes) and without the need of any partial derivatives. Hence, lots of numerical problems of partial derivatives on discrete grids can be avoided. We gave formal as well as experimental proofs of our results. The *conformal monogenic signal* shows the natural relation of the original image domain to geometric entities such as lines, circles, hyperplanes and hyperspheres.

References

1. Carneiro, G., Jepson, A.D.: Phase-based local features. In: 7th European Conference on Computer Vision-Part I. LNCS, vol. 2350, pp. 282–296. Springer, Berlin, Heidelberg, New York (2002)
2. Coope, I.D.: Circle fitting by linear and nonlinear least squares. J. Optim. Theory Appl. **76**(2), 381–388 (1993)
3. do Carmo, M.P.: Differential Geometry of Curves and Surfaces. Prentice-Hall, New York (1976)
4. Felsberg, M., Sommer, G.: The monogenic signal. IEEE Trans. Signal Process. **49**(12), 3136–3144 (2001)
5. Felsberg, M., Sommer, G.: The monogenic scale-space: a unifying approach to phase-based image processing in scale-space. J. Math. Imaging Vis. **21**, 5–26 (2004)
6. Fleet, D.J., Jepson, A.D.: Stability of phase information. IEEE Trans. Pattern Anal. Mach. Intell. **15**(12), 1253–1268 (1993)
7. Fleet, D.J., Jepson, A.D., Jenkin, M.R.M.: Phase-based disparity measurement. CVGIP, Image Underst. **53**, 198–210 (1991)
8. Gabor, D.: Theory of communication. J. IEE (Lond.) **93**, 429–457 (1946)
9. Gander, W., Golub, G.H., Strebel, R.: Least-squares fitting of circles and ellipses. BIT **34**(4), 558–578 (1994)
10. Huang, T., Burnett, J., Deczky, A.: The importance of phase in image processing filters. IEEE Trans. Acoust. Speech Signal Process. **23**(6), 529–542 (1975)
11. Krause, M., Sommer, G.: A 3D isotropic quadrature filter for motion estimation problems. In: Proc. Visual Communications and Image Processing, Beijing, China, vol. 5960, pp. 1295–1306. The International Society for Optical Engineering, Bellingham (2005)
12. Lichtenauer, J., Hendriks, E.A., Reinders, M.J.T.: Isophote properties as features for object detection. CVPR (2), 649–654 (2005)
13. Luo, Y., Al-Dossary, S., Marhoon, M., Alfaraj, M.: Generalized Hilbert transform and its applications in geophysics. Lead. Edge **22**(3), 198–202 (2003)
14. Oppenheim, A.V., Lim, J.S.: The importance of phase in signals. Proc. IEEE **69**(5), 529–541 (1981)
15. Romeny, B.M. (ed.): Geometry-Driven Diffusion in Computer Vision. Kluwer Academic, Dordrecht (1994)
16. Stein, E.M.: Singular Integrals and Differentiability Properties of Functions (PMS-30). Princeton University Press, Princeton (1971)
17. van de Weijer, J., van Vliet, L.J., Verbeek, P.W., van Ginkel, M.: Curvature estimation in oriented patterns using curvilinear models applied to gradient vector fields. In: IEEE Transactions on Pattern Analysis and Machine Intelligence, vol. 23, pp. 1035–1042 (2001)
18. van Ginkel, M., van de Weijer, J., van Vliet, L.J., Verbeek, P.W.: Curvature estimation from orientation fields. In: Ersboll, B.K. (ed.) 11th Scandinavian Conference on Image Analysis, pp. 545–551. Pattern Recognition Society of Denmark (1999)
19. Wietzke, L., Sommer, G.: The signal multi-vector. J. Math. Imaging Vis. **37**, 132–150 (2010)
20. Xiaoxun, Z., Yunde, J.: Local Steerable Phase (LSP) feature for face representation and recognition. In: CVPR'06: Proceedings of the 2006 IEEE Computer Society Conference on Computer Vision and Pattern Recognition, pp. 1363–1368. IEEE Comput. Soc., Los Alamitos (2006)
21. Zang, D., Wietzke, L., Schmaltz, C., Sommer, G.: Dense optical flow estimation from the monogenic curvature tensor. In: Scale Space and Variational Methods. LNCS, vol. 4485, pp. 239–250. Springer, Berlin, Heidelberg, New York (2007)
22. Zetzsche, C., Barth, E.: Fundamental limits of linear filters in the visual processing of two-dimensional signals. Vis. Res. **30**, 1111–1117 (1990)
23. Zhang, L., Qian, T., Zeng, Q.: Radon measure formulation for edge detection using rotational wavelets. Commun. Pure Appl. Anal. **6**(3), 899–915 (2007)

Oliver Fleischmann received a diploma degree in computer science from the Christian-Albrechts-University of Kiel, Germany, 2008. He is currently a Ph.D. candidate in the Cognitive Systems Group at the Department of Computer Science at the Christian-Albrechts-University of Kiel, Germany. His research interests include signal processing, pattern recognition, parameter estimation, and low level image processing.

Lennart Wietzke received a diploma degree in computer science from the Technical-University of Clausthal, Germany, 2005. He is currently a Ph.D. candidate at the Department of Computer Science at the Christian-Albrechts-University of Kiel, Germany. His research interests include pattern recognition and low level signal analysis. Since 2009, together with his partner Christian Perwass he is the CEO of the company Raytrix GmbH, which has focused on computational photography, plenoptic cameras and software for industrial and scientific applications (www.raytrix.de).

Gerald Sommer received a diploma degree in physics from Friedrich-Schiller-University Jena, Germany, in 1969, a Ph.D. degree in physics from the same university in 1975, and a habilitation degree in engineering from Technical University Ilmenau, Germany, in 1988. From 1969 to 1991 he worked at several departments of the Friedrich-Schiller-University Jena. From 1991 to 1993, he was the head of the division for medical image processing at the Research Center for Environment and Health (GSF-Medis) in Munich-Neuherberg. Since 1993, he is a professor at the Department of Computer Science and at the Christian Albrechts University of Kiel, Germany. He is leading the research group Cognitive Systems. The research covers signal theory and signal processing, neural computation for pattern recognition, computer vision and robot control.